J. Fluid Mech. (2019), *vol.* 871, *pp.* 636–667. © Cambridge University Press 2019
doi:10.1017/jfm.2019.320

Nanoparticle diffusion in sheared cellular blood flow

Zixiang Liu[1], Jonathan R. Clausen[3], Rekha R. Rao[3] and Cyrus K. Aidun[1,2,†]

[1]George W. Woodruff School of Mechanical Engineering, Georgia Institute of Technology, Atlanta, GA 30332, USA

[2]Parker H. Petit Institute for Bioengineering and Bioscience, Georgia Institute of Technology, Atlanta, GA 30332, USA

[3]Sandia National Laboratories, Albuquerque, NM 87185, USA

(Received 12 November 2018; revised 25 March 2019; accepted 8 April 2019; first published online 24 May 2019)

Using a multiscale blood flow solver, the complete diffusion tensor of nanoparticles (NPs) in sheared cellular blood flow is calculated over a wide range of shear rate and haematocrit. In the short-time regime, NPs exhibit anomalous dispersive behaviors under high shear and high haematocrit due to the transient elongation and alignment of the red blood cells (RBCs). In the long-time regime, the NP diffusion tensor features high anisotropy. Particularly, there exists a critical shear rate ($\sim$100 s^{-1}) around which the shear-rate dependence of the diffusivity tensor changes from linear to nonlinear scale. Above the critical shear rate, the cross-stream diffusivity terms vary sublinearly with shear rate, while the longitudinal term varies superlinearly. The dependence on haematocrit is linear in general except at high shear rates, where a sublinear scale is found for the vorticity term and a quadratic scale for the longitudinal term. Through analysis of the suspension microstructure and numerical experiments, the nonlinear haemorheological dependence of the NP diffusion tensor is attributed to the streamwise elongation and cross-stream contraction of RBCs under high shear, quantified by a capillary number. The RBC size is shown to be the characteristic length scale affecting the RBC-enhanced shear-induced diffusion (RESID), while the NP submicrometre size exhibits negligible influence on the RESID. Based on the observed scaling behaviours, empirical correlations are proposed to bridge the NP diffusion tensor to specific shear rate and haematocrit. The characterized NP diffusion tensor provides a constitutive relation that can lead to more effective continuum models to tackle large-scale NP biotransport applications.

Key words: blood flow, particle/fluid flow, suspensions

1. Introduction

The rapid advancement of nanotechnology and nanomaterial manufacturing has led to emerging exposure of human biological systems, such as cardiovascular systems, to nanosized particulate matter (Albanese, Tang & Chan 2012; Malysheva, Lombi &

† Email address for correspondence: cyrus.aidun@me.gatech.edu

https://doi.org/10.1017/jfm.2019.320 Published online by Cambridge University Press

Voelcker 2015), ranging from engineered nanocarriers functioning as medicine/imaging agents (Yoo *et al.* 2011; Blanco, Shen & Ferrari 2015; Griffin *et al.* 2018) to aerosol pollutant particulates potentially causing fatal cardiovascular disease (Brook *et al.* 2010; Newby *et al.* 2015; Miller *et al.* 2017). Both the design of optimal nanocarrier systems and the prevention and control of nanoparticle (NP) toxicity rely heavily on the knowledge of NP distribution in vascular systems (Albanese *et al.* 2012). Nevertheless, the biodistribution of NPs remains elusive to date and limits the bioavailability of NP systems to the human bio-environment. One of the primary bottlenecks is the lack of understanding on the NP dispersive mechanisms in blood flow with respect to specific haemorheological conditions.

Multiscale computational models (Lee *et al.* 2013; Muller, Fedosov & Gompper 2014; Liu *et al.* 2018) have been developed and applied to predict the NP distribution in microvessels by directly simulating NPs and red blood cells (RBCs) suspended in blood plasma. Although these models, as particle-based approaches, provide a straightforward means to predict the NP distribution in realistic, microscale vessels, they are still computationally intractable when it comes to organ- and circulation-level applications. Alternatively, continuum models (Eckstein & Belgacem 1991; Decuzzi *et al.* 2010; Hossain *et al.* 2013; Mehrabadi, Ku & Aidun 2015) have the ability to predict NP distribution in large-scale vascular systems by solving the three-dimensional (3D) convection–diffusion equation

$$\frac{\partial c}{\partial t} + \boldsymbol{u} \cdot \nabla c + \nabla \cdot \boldsymbol{J} = 0, \tag{1.1}$$

where t is time, c is the NP concentration, $\boldsymbol{u}$ is the local fluid velocity and $\boldsymbol{J}$ is the flux of NP concentration. Here, $\boldsymbol{J}$ is often estimated by Fick's law as $\boldsymbol{J} = -\boldsymbol{D}^{\infty} \cdot \nabla c$, where the NP diffusion tensor, $\boldsymbol{D}^{\infty}$, has so far been treated as isotropic, Brownian diffusivity (Hossain *et al.* 2013) or solute diffusivity measured in a single principal direction (Zydney & Colton 1988). Since the particle diffusion tensor is anisotropic in nature even for monodisperse rigid-sphere suspensions (Foss & Brady 1999, 2000*b*), an improved constitutive relation capturing the anisotropy of $\boldsymbol{D}^{\infty}$ subject to local haemorheological properties is therefore necessary to form a better closure of this convection–diffusion problem.

Using Couette-type flow devices, experiments have been conducted to characterize the particle self-diffusivity (Eckstein, Bailey & Shapiro 1977; Breedveld *et al.* 1998) and effective solute diffusivity (Wang & Keller 1985; Zydney & Colton 1988; Breedveld *et al.* 1998) in non-colloidal particle suspensions under linear shear flow for various shear rates and particle volume fractions. However, due to the difficulties of particle tracking in the presence of the affine flow effect, only the particle diffusivity in the cross-stream directions are reported. Apart from the experimental efforts, particle-scale simulations have become an important tool for characterizing the anisotropic particle diffusivity tensor in both colloidal (Foss & Brady 1999, 2000*a*,*b*) and non-colloidal (Sierou & Brady 2004; Yeo & Maxey 2010; Clausen, Reasor & Aidun 2011) suspensions under shear flow. Owing to the success of those particle-scale simulation techniques, substantial progress has been made in understanding the rheological and hydrodynamic responses of the particle diffusion tensor in sheared monodisperse suspensions. Nonetheless, the bidisperse RBC–NP suspension system remains largely unexplored and entails unique transport phenomenology that is unavailable to the conventional monodisperse particle suspensions.

https://doi.org/10.1017/jfm.2019.320 Published online by Cambridge University Press

First, there is a large discrepancy in length scale between NPs ($\sim O(10\ \text{nm})$) and RBCs ($\sim O(10\ \mu\text{m})$). Consequently, NPs are subject to both molecular-level thermal fluctuations (Brownian motion) and cellular-level interactions with RBCs. On macroscopic scales, the two effects synergistically give rise to an apparent diffusivity contributed by both Brownian diffusivity (BD) and the so-called RBC-enhanced shear-induced diffusivity (RESID) (Mehrabadi *et al.* 2015; Mehrabadi, Ku & Aidun 2016; Liu *et al.* 2018). Second, the NP phase shows infinite dilution while the RBC phase exhibits a range of physiological concentrations from $\sim 10\,\%$ to $\sim 40\,\%$. Consequently, the BD shows insignificant dependence on shear rate and haematocrit, while the RESID is highly dependent on the haemorheological conditions (Mehrabadi *et al.* 2016). Third, RBCs deform considerably under shear, from biconcave shape in equilibrium to large elongation and tank treading of the membrane under high shear (Gross, Kruger & Varnik 2014). Such geometric asymmetry and morphological changes of RBCs could alter RESID substantially.

Therefore, the objective of the present work is to characterize the bulk diffusivity tensor of NP in sheared blood flow and interrogate the NP dispersive mechanism specific to a broad range of haematocrit and shear rate. Given the large length-scale discrepancy (three to four orders of magnitude) between NP and RBC, resolving both particle phases using direct numerical simulation (DNS) is computationally prohibitive. Therefore, a multiscale complex blood flow solver (Aidun & Clausen 2010; Reasor, Clausen & Aidun 2012, 2013*a*; Liu *et al.* 2018, 2019) is employed to treat NPs as effective Brownian particles while directly resolving the RBC phase. Such a multiscale treatment can substantially reduce the computational expense but still preserve the critical suspension physics at distinct scales. As will be shown in the following section (§ 3.3.1), good comparison between the simulation and experimental results can be obtained using this multiscale approach. Since confinement (wall) effects in general lead to spatial heterogeneity of the blood flow (Kumar & Graham 2012) that forbids the calculation of NP diffusivity related to specific haematocrit and shear rate, the Lees–Edwards boundary condition (LEbc) (Lees & Edwards 1972) is implemented (MacMeccan *et al.* 2009) to impose unconfined simple shear flow to obtain the NP bulk diffusive properties.

Note that blood flow typically occurs under confinement (e.g. blood flow in arteries) involving heterogeneous flow structures that could induce cell segregation (Kumar & Graham 2012; Ahmed *et al.* 2018) and margination (Zhao & Shaqfeh 2011; Zhao, Shaqfeh & Narsimhan 2012; Reasor *et al.* 2013*b*; Mehrabadi *et al.* 2015, 2016). Such phenomena are found to be a synergistic outcome of the RBC-induced diffusion in the RBC-laden region and the formation of a cell-free layer (CFL) near the wall (Mehrabadi *et al.* 2015, 2016). For NPs with negligible inertia and much smaller length scale compared to the CFL thickness (Zhao *et al.* 2012; Mehrabadi *et al.* 2016), it is expected that the presence of the wall has an insignificant direct influence on the NP diffusion in the RBC-laden region. Besides, large-scale problems suitable for continuum modelling (such as blood flow through coronary arteries) typically feature much larger length and time scales compared to those considered in the current cellular-scale studies. It is therefore plausible to hypothesize that the long-time NP diffusion tensor evaluated in an unbounded simple shear flow should closely capture the NP diffusive behaviour subject to the same local haemorheological condition in a macroscale heterogeneous blood flow environment.

One unique contribution of this work is the development of a multiscale-simulation-informed empirical expression that links the anisotropic NP diffusion tensor to the local haemorheological conditions. Such 3D NP diffusive information in sheared

https://doi.org/10.1017/jfm.2019.320 Published online by Cambridge University Press

blood is intractable to measure through either experiment or DNS simulation. On the application side, the developed NP diffusion tensor provides a constitutive relation that can lead to more effective continuum-level models to tackle large-scale NP biotransport problems. On the suspension rheology side, the diffusive phenomenology observed in such a biophysical, bidisperse RBC–NP suspension system could entail novel suspension physics that is unavailable to conventional suspension flows.

The remainder of this article is organized as follows. In § 2, the details of the computational methodology are presented. In § 3, we present results and perform numerical experiments. In § 3.1, the numerical problem is formulated with careful consideration of numerical resolution as well as physiological significance. In § 3.2, the transient dispersive behaviours of NPs are presented. As follows in § 3.3, the long-time diffusive behaviours of NPs subject to a wide range of shear rate and haematocrit are validated with available experimental data and interrogated with various haemorheological scaling behaviours. In § 3.4, the NP–RBC suspension microstructure is analysed to give mechanistic insights into the haemorheological scaling observations. In §§ 3.5 and 3.6, numerical experiments are conducted to shed light on the physical mechanisms governing the nonlinear shear-rate dependence of the NP diffusion tensor. In § 3.7, empirical correlations are proposed based on the haemorheological scalings observed in previous sections. In § 4, we conclude this work with some remarks.

2. Methodology

The numerical method for this study is through a 3D lattice-Boltzmann (LB) based multiscale complex blood flow solver that efficiently resolves both the dynamics and interactions of nanoscale particles and microscale capsules (Aidun, Lu & Ding 1998; Aidun & Qi 1998; Aidun & Clausen 2010; Reasor *et al.* 2012; Liu *et al.* 2018, 2019), as demonstrated in figure 1. The LB method is a well-established numerical model for hydrodynamics and proves to be a highly scalable method for DNS of dense particulate suspensions (Aidun & Clausen 2010; Clausen, Reasor & Aidun 2010). Modelling of the RBC dynamics and deformation is via a coarse-grained spectrin-link membrane method (Pivkin & Karniadakis 2008; Fedosov, Caswell & Karniadakis 2010) coupled to the LB method (Reasor *et al.* 2012), which has been validated against experimental results (Reasor *et al.* 2012, 2013*a*). The NP suspension dynamics are resolved via a two-way coupled lattice-Boltzmann Langevin-dynamics (LB-LD) method with both particle Brownian motion and long-range hydrodynamic interactions (HI) directly resolved and validated (Liu *et al.* 2018, 2019). The solver has been successfully applied to several studies of particle and biopolymer transport in cellular blood flow (Reasor *et al.* 2013*a*,*b*; Mehrabadi *et al.* 2016; Ahmed *et al.* 2018; Griffin *et al.* 2018; Liu *et al.* 2018).

2.1. *Lattice-Boltzmann method*

Simulation of the suspending fluid is based on the LB method developed by Aidun & Lu (1995), Aidun *et al.* (1998) and Aidun & Clausen (2010). The LB method solves the discretized Boltzmann transport equation in velocity space through the streaming–collision process. In streaming, the fictitious fluid particles propagate along discrete velocity vectors forming a lattice space. In collision, the fluid particles at each lattice site collide with each other, causing the relaxation of the particle distribution function (PDF) towards a local 'Maxwellian' equilibrium PDF. The collision term is linearized based on the single-relaxation-time Bhatnagar–Gross–Krook (BGK) operator

https://doi.org/10.1017/jfm.2019.320 Published online by Cambridge University Press

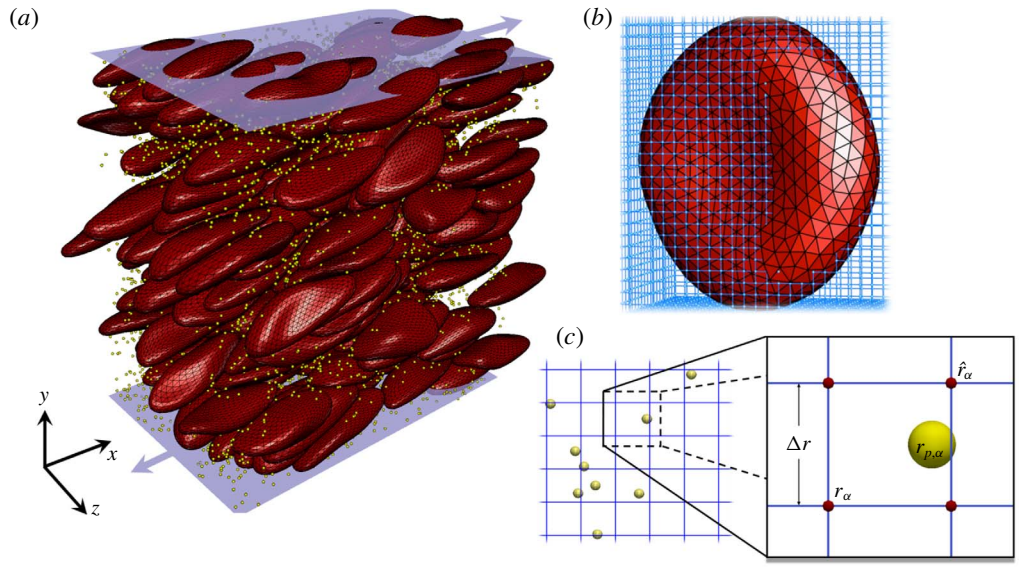


FIGURE 1. (Colour online) (*a*) The RBC–NP bidisperse suspension in a triply periodic domain at shear rate $\dot{\gamma} = 1000\ \mathrm{s}^{-1}$ and haematocrit $\phi = 40\,\%$. (*b*) The RBC membrane immersed in the LB lattice domain. The RBC membrane dynamics and deformation are captured by the course-grained spectrin-link method (Pivkin & Karniadakis 2008; Fedosov *et al.* 2010; Reasor *et al.* 2012). (*c*) The NP suspension dynamics is captured by the LB-LD method (Liu *et al.* 2018, 2019), which captures the NP Brownian motion and long-range HI in an off-lattice fashion.

(Bhatnagar, Gross & Krook 1954). The temporal evolution of the particle distribution function is given as

$$f_i(\boldsymbol{r} + \Delta t\, \boldsymbol{e}_i, t + \Delta t) = f_i(\boldsymbol{r}, t) - \frac{\Delta t}{\tau}[f_i(\boldsymbol{r}, t) - f_i^{(0)}(\boldsymbol{r}, t)] + f_i^S(\boldsymbol{r}, t), \tag{2.1}$$

where f_i is the fluid PDF, $f_i^{(0)}$ is the equilibrium PDF, r is the lattice site, e_i is the discrete lattice velocity, t is time, τ is the single relaxation time and f_i^S is a forcing source term introduced to account for the discrete external force effect (He *et al.* 1997). This method has a pseudo speed of sound, $c_s = \Delta r/(\sqrt{3}\Delta t)$, and a fluid kinematic viscosity, $\nu = (\tau - \Delta t/2)c_s^2$, where Δt is the time step and Δr is the unit lattice distance. The positivity of ν requires $\tau > \Delta t/2$. In the LB method, time and space are typically normalized by Δt and Δr, respectively, such that $\Delta t_{LB} = \Delta r_{LB} = 1$ are employed to advance equation (2.1). In the near-incompressible limit (i.e. Mach number, $Ma = u/c_s \ll 1$), the LB equation recovers the Navier–Stokes equation (Junk & Yong 2003) with the equilibrium PDF given in terms of local macroscopic variables as

$$f_i^{(0)}(\boldsymbol{r}, t) = \omega_i \rho \left[1 + \frac{1}{c_s^2}(\boldsymbol{e}_i \cdot \boldsymbol{u}) + \frac{1}{2c_s^4}(\boldsymbol{e}_i \cdot \boldsymbol{u})^2 - \frac{1}{2c_s^2}(\boldsymbol{u} \cdot \boldsymbol{u})\right], \tag{2.2}$$

where ω_i denotes the set of lattice weights defined by the LB stencil in use. The macroscopic properties such as the fluid density ρ, velocity $\boldsymbol{u}$ and pressure p are

https://doi.org/10.1017/jfm.2019.320 Published online by Cambridge University Press

obtained via moments of the equilibrium distribution functions as

$$\rho = \sum_{i=1}^{Q} f_i^{(0)}(\boldsymbol{r}, t), \quad \boldsymbol{u} = \frac{1}{\rho}\sum_{i=1}^{Q} f_i^{(0)}(\boldsymbol{r}, t)\boldsymbol{e}_i, \quad p\boldsymbol{I} = \sum_{i=1}^{Q} f_i^{(0)}(\boldsymbol{r}, t)\boldsymbol{e}_i\boldsymbol{e}_i - \rho\boldsymbol{u}\boldsymbol{u}, \qquad (2.3a\text{–}c)$$

respectively. Here, $\boldsymbol{I}$ is the identity tensor, and pressure can be related to density and the speed of sound through $p = \rho c_s^2$. For the D3Q19 stencil adopted in the current study, Q is equal to 19. Along the rest, non-diagonal and diagonal lattice directions, ω_i is equal to 1/3, 1/18 and 1/36, and $|\boldsymbol{e}_i|$ is equal to 0, $\Delta r/\Delta t$ and $\sqrt{2}(\Delta r/\Delta t)$, correspondingly.

2.2. *Spectrin-link method*

Modelling of the RBC membrane is through a coarse-grained spectrin-link (SL) method (Pivkin & Karniadakis 2008; Fedosov *et al.* 2010) coupled with the LB method, which has been extensively validated with experimental results and proved to be a successful tool to capture both single RBC deformation and dynamics (Reasor *et al.* 2012) and rheology of RBC suspensions at physiological haematocrit (Reasor *et al.* 2013*a*). In the SL model, the RBC membrane is modelled as a triangulated network with a collection of vertices mimicking actin vertex coordinates, denoted by $\{\boldsymbol{x}_n, n \in 1, \ldots, N\}$. The Helmholtz free energy of the network system, $E(\boldsymbol{x}_n)$, including in-plane, bending, volume and surface area energy components (Dao, Li & Suresh 2006), is given by

$$E(\boldsymbol{x}_n) = E_{IP} + E_B + E_\Omega + E_A. \qquad (2.4)$$

Here, the in-plane energy, E_{IP}, characterizes the membrane shear modulus through a worm-like chain (WLC) potential (Bustamante, Bryant & Smith 2003) coupled with a hydrostatic component (Fedosov *et al.* 2010). The bending energy, E_B, specifies the membrane bending stiffness, which is essential in characterizing the equilibrium RBC biconcave morphology (Dao *et al.* 2006; Fedosov *et al.* 2010). The volumetric constraint energy, E_Ω, and the area constraint energy, E_A, preserve the RBC volume and area conservation, respectively, when subject to external forces.

The dynamics of each vertex advance according to Newton's equations of motion,

$$\frac{\mathrm{d}\boldsymbol{x}_n}{\mathrm{d}t} = \boldsymbol{v}_n, \quad M\frac{\mathrm{d}\boldsymbol{v}_n}{\mathrm{d}t} = \boldsymbol{f}_n^{SL} + \boldsymbol{f}_n^{LB} + \boldsymbol{f}_n^{CC}, \qquad (2.5a,b)$$

where $\boldsymbol{v}_n$ is the velocity of the vertex n, and M is the fictitious mass equal to the total mass of the cell divided by the number of vertices N. The number of vertices used to discretize the RBC membrane is $N = 613$, which has been shown to yield adequate resolution to resolve hydrodynamic forces (MacMeccan *et al.* 2009) and capture single RBC dynamics (Reasor *et al.* 2012) and concentrated RBC suspension rheology (Reasor *et al.* 2013*a*) when coupled with the LB method. Force $\boldsymbol{f}_n^{LB}$ specifies the forces on the vertex due to the fluid–solid coupling; $\boldsymbol{f}_n^{CC}$ are the forces due to cell–cell interactions; and the forces due to the Helmholtz free energy based on the SL model are determined by

$$\boldsymbol{f}_n^{SL} = -\frac{\partial E(\boldsymbol{x}_n)}{\partial \boldsymbol{x}_n}. \qquad (2.6)$$

The SL method is solved by integrating equations (2.5) at each LB time step using a first-order-accurate forward Euler scheme that is consistent with the LB evolution equation to avoid excessive computational expense (Reasor *et al.* 2012; Liu *et al.* 2018).

https://doi.org/10.1017/jfm.2019.320 Published online by Cambridge University Press

2.3. *Langevin dynamics approach*

The nanoscale particle suspensions are resolved through a two-way coupled LB-LD method (Liu *et al.* 2018, 2019), which has been shown to correctly capture the theoretical Brownian diffusivity and long-range many-body HI. This approach treats suspended particles in Stokesian regimes as point particles, while the particles with Brownian effect are coupled to the non-fluctuating LB fluid in a two-way fashion through spatial extrapolation/interpolation schemes (Ahlrichs & Dünweg 1999; Peskin 2002; Mynam, Sunthar & Ansumali 2011). The dynamics of the LD particles is described by the Langevin equation (LE),

$$m\frac{\mathrm{d}\boldsymbol{u}_p}{\mathrm{d}t} = \boldsymbol{C}_p + \boldsymbol{F}_p + \boldsymbol{S}_p, \tag{2.7}$$

where m is the mass of a single particle. The conservative force $\boldsymbol{C}_p$, specifying the interparticle and particle–surface interaction forces, is determined by calculating the directional derivatives of the total potential energy U_{total} as

$$\boldsymbol{C}_p = -\frac{\mathrm{d}U_{total}}{\mathrm{d}\boldsymbol{r}_p}, \tag{2.8}$$

where the details of U_{total} are discussed in § 2.5. The frictional force $\boldsymbol{F}_p$ is assumed to be proportional to the relative velocity of the particle with respect to the local viscous fluid velocity (Ahlrichs & Dünweg 1998, 1999),

$$\boldsymbol{F}_p = -\zeta[\boldsymbol{u}_p(t) - \boldsymbol{u}(\boldsymbol{r}_p, t)], \tag{2.9}$$

where $\boldsymbol{u}_p$ denotes the particle velocity, and $\boldsymbol{u}(\boldsymbol{r}_p, t)$ is the interpolated LB fluid velocity at the centre of the particle. The friction coefficient ζ is determined by the Stokes' drag law, $\zeta = 3\pi\mu d_p$, where μ is the dynamic viscosity of the suspending fluid. The stochastic force $\boldsymbol{S}_p$ explicitly gives rise to the Brownian motion of the particle and satisfies the fluctuation–dissipation theorem (FDT) (Kubo 1966) by

$$\langle S^{\alpha}_{p,i}(t)\rangle = 0, \quad \langle S^{\alpha}_{p,i}(t) S^{\beta}_{p,j}(t)\rangle = 2k_B T\zeta\,\delta_{ij}\delta_{\alpha\beta}\delta(t-t'), \tag{2.10}$$

where $i, j \in \{x, y, z\}$, α and β run through all the particle indices, δ_{ij} and $\delta_{\alpha\beta}$ are Kronecker deltas, $\delta(t-t')$ is the Dirac delta function, k_B is the Boltzmann constant and T is the absolute temperature of the suspending fluid. The angle brackets denote the ensemble average over all the realizations of the random variables. Since only time scales equal to and greater than the Brownian diffusion time scale are of interest, this study solves the overdamped discretized LE as suggested in Liu *et al.* (2018, 2019).

2.4. *Fluid–solid coupling*

The coupling between fluid and RBC is accomplished through the Aidun–Lu–Ding (ALD) fluid–solid interaction approach, the details of which are well documented in previous publications (Aidun *et al.* 1998; Aidun & Clausen 2010; Reasor *et al.* 2012). To resolve the NP dynamics subject to the hydrodynamics and the long-range HI among NPs, the LD particle and the non-fluctuating LB fluid phase are coupled in a two-way fashion, as discussed and verified in previous studies (Mynam *et al.* 2011; Liu *et al.* 2018, 2019). Specifically, the hydrodynamic force exerted on an NP, $\boldsymbol{F}^H_p$, is systematically decomposed into frictional and stochastic components as

$$\boldsymbol{F}^H_p = \boldsymbol{F}_p + \boldsymbol{S}_p = -\zeta[\boldsymbol{u}_p(t) - \boldsymbol{u}(\boldsymbol{r}_p, t)] + \boldsymbol{S}_p, \tag{2.11}$$

https://doi.org/10.1017/jfm.2019.320 Published online by Cambridge University Press

where the fluid velocity at the particle site, $\boldsymbol{u}(\boldsymbol{r}_p, t)$, is interpolated based on the surrounding LB velocities and applied to update the LD particle dynamics through equation (2.7). The weighting functions, $w(\boldsymbol{r}, \boldsymbol{r}_p)$, for interpolation are constructed using a trilinear scheme (Ahlrichs & Dünweg 1998; Liu *et al.* 2018). Since $\boldsymbol{F}_p$ and $\boldsymbol{S}_p$ both originate from the 'collision' between NPs and liquid molecules, $\boldsymbol{F}_p^H$ (instead of $\boldsymbol{F}_p$) is assigned back to the fluid phase to satisfy momentum conservation. The same weighting function is then applied to constructing the local forcing source term as

$$f_i^S(\boldsymbol{r}, t) = -\frac{w(\boldsymbol{r}, \boldsymbol{r}_p)\omega_i \boldsymbol{F}_p^H \cdot \boldsymbol{e}_i}{c_s^2 \Delta r^3}, \tag{2.12}$$

which is adopted by equation (2.1) to update the local hydrodynamics. The coupled LB-LD method, similar to the external boundary force (EBF) method (Wu & Aidun 2010), modifies the conventional LB evolution equation into equation (2.1) by adding the forcing distribution function $f_i^S(\boldsymbol{r}, t)$, which is shown to approximate the Navier–Stokes equation in the macroscopic scale (Guo, Zheng & Shi 2002).

2.5. *Contact modelling*

The contact model for RBCs that specifies $\boldsymbol{f}_n^{CC}$ is based on the subgrid contact functions originally formulated in Ding & Aidun (2003) and later improved by MacMeccan *et al.* (2009) and Clausen *et al.* (2011). It prevents the RBC from overlapping when cell–cell membrane separation is below one LB lattice spacing. In this model, the lubrication term is replaced with an exponential contact function to avoid numerical instability driven by the singular nature of the lubrication hydrodynamics and the discrete nature of the interparticle separation calculation, as explained in detail in MacMeccan *et al.* (2009) and Clausen & Aidun (2010). The rheological insensitivity of the contact model to model parameters has been discussed in detail by Clausen *et al.* (2011). This contact model has also been previously applied in the characterization of the rheological properties of concentrated deformable capsule (Clausen *et al.* 2011) and RBC (Reasor *et al.* 2013*a*) suspensions with satisfactory agreement with experimental measurements. Although the lubrication force is shown to play some role in particle self-diffusion in sheared monodisperse rigid-particle suspensions (Foss & Brady 2000*a*,*b*), we anticipate such an effect to be insignificant in the current bidisperse suspension system given that NP diffusion is dominated by the RBC–NP interactions.

The NP–RBC contact model that provides U_{total} is based on the Morse potential documented in Liu *et al.* (2004), which is an empirical model for particle–particle interactions that can be calibrated to match experimental measurements (Neu & Meiselman 2002; Liu *et al.* 2004). Owing to the variety and somewhat lack of statistics for actual NP–RBC short-distance interaction, this study employs the measured cell–cell interaction potential (Neu & Meiselman 2002) for the NP–RBC interactions. The potential parameters are specified according to Liu *et al.* (2004) but with a cutoff distance selected to preserve only the repulsive effect. The detailed formulation of the Morse potential has been discussed in appendix A with sensitivity analysis performed showing that the computation of NP diffusivity is insensitive to the change of the model parameters up to 60 %. This suggests that the NP diffusion is largely driven by the hydrodynamic interaction rather than by the direct contact between NP and RBC membrane. The short-distance NP–NP interaction is neglected due to the extreme dilution of the NP concentration ($\ll 1$ %) considered.

https://doi.org/10.1017/jfm.2019.320 Published online by Cambridge University Press

This work does not attempt to model any adhesive forces between RBCs since above the shear rate of 5 s^{-1} the aggregation of RBCs is not significant (Fedosov *et al.* 2011). Although the adhesion or uptake of NPs to cells may be influential to the NP dispersive behaviour (Shang, Nienhaus & Nienhaus 2014), it is however not within the scope of this study.

2.6. *Lees–Edwards boundary condition*

Since the primary focus of this study is on the particle bulk diffusive behaviour subject to no wall effect, simulations are performed in an unbounded, triply periodic cubic domain where a constant shear rate is imposed through the Lees–Edwards boundary condition (LEbc) (Lees & Edwards 1972). This method, originally developed for molecular dynamics simulations, was extended to the LB method by Wagner & Pagonabarraga (2002) and later applied to deformable suspensions on parallel computing architectures by Clausen *et al.* (2011) and Reasor *et al.* (2013*a*). In addition to the operations associated with regular periodic boundary conditions, both the particle (NP and RBC) phase and the fluid phase undergo a shift in position and velocity according to the LEbc scheme as they cross the top ($+y$) or bottom ($-y$) boundary.

2.7. *Characterization of the particle diffusion tensor*

The presence of shearing flow imposes a convective effect on the particle suspension and complicates the characterization of particle diffusion tensor. The major difficulty lies in determination of the longitudinal diffusivity (D^{∞}_{xx}) and off-diagonal diffusivity (D^{∞}_{xy}), which require careful subtraction of the affine particle displacement. The diffusion tensor in sheared monodisperse colloidal suspensions has been successfully quantified by sampling the non-affine particle mean-square displacements (MSDs) (Morris & Brady 1996; Foss & Brady 1999, 2000*b*; Zia & Brady 2010). Therefore, this study calculates the long-time NP diffusion tensor, $\boldsymbol{D}^{\infty}$, in the form of

$$\boldsymbol{D}^{\infty} = \begin{pmatrix} D^{\infty}_{xx} & D^{\infty}_{xy} & 0 \\ D^{\infty}_{yx} & D^{\infty}_{yy} & 0 \\ 0 & 0 & D^{\infty}_{zz} \end{pmatrix}, \tag{2.13}$$

where each non-zero diffusion component is calculated by

$$D^{\infty}_{xx} = \frac{1}{2}\frac{\mathrm{d}}{\mathrm{d}t}[\langle x^{na}(t)x^{na}(t)\rangle - \langle x^{na}(t)\rangle\langle x^{na}(t)\rangle], \tag{2.14a}$$

$$D^{\infty}_{xy} = \frac{1}{2}\frac{\mathrm{d}}{\mathrm{d}t}[\langle x^{na}(t)y(t)\rangle - \langle x^{na}(t)\rangle\langle y(t)\rangle], \tag{2.14b}$$

$$D^{\infty}_{yy} = \frac{1}{2}\frac{\mathrm{d}}{\mathrm{d}t}[\langle y(t)y(t)\rangle - \langle y(t)\rangle\langle y(t)\rangle], \tag{2.14c}$$

$$D^{\infty}_{zz} = \frac{1}{2}\frac{\mathrm{d}}{\mathrm{d}t}[\langle z(t)z(t)\rangle - \langle z(t)\rangle\langle z(t)\rangle], \tag{2.14d}$$

as $t \to \infty$. Here, and hereinafter, the angle brackets denote an ensemble average over all NPs in the system; x, y and z denote the absolute displacement of the NP in the three principal flow directions, i.e. longitudinal, velocity-gradient and vorticity directions, respectively. The diffusivity tensor is symmetric, thus D^{∞}_{xy} and

https://doi.org/10.1017/jfm.2019.320 Published online by Cambridge University Press

D^{∞}_{yx} are equal; D^{∞}_{xz} and D^{∞}_{yz} (and their transposes) are insignificant (Brady & Morris 1997), which is also confirmed in our simulation. The non-affine displacement, x^{na}, is calculated by subtracting the absolute displacement with its affine component, x^{a}, i.e. $x^{na}(t) = x(t) - x^{a}(t)$, where $x^{a}(t) = \int_0^t \dot{\gamma} y(\tau)\,\mathrm{d}\tau$, and $\dot{\gamma}$ is the imposed shear rate through LEbc. When calculating the absolute displacement of NPs that undergo a shift of position due to the LEbc, the particle reference position is shifted accordingly to subtract the shift effect. Particle displacements are followed every $\sim 0.06\dot{\gamma}t$ to ensure that the growth of MSDs is captured with adequate accuracy. For clarity, the superscript of the affine displacement and the expectation terms are both dropped in the MSD notation as follows.

3. Results

In this section, we first formulate the simulations based on both physiological and numerical rationales. As follows, the transient growth of the NP mobility is discussed to understand the short-time response of the NP dispersive behaviour at various haematocrits and shear rates. Then, focus will be shifted to understanding the NP long-time diffusive behaviour under different haemorheological conditions with appropriate scaling, where the simulation results are also compared with available experimental data. To gain insight into the mechanisms governing the nonlinear haematocrit and shear-rate dependence of the NP diffusion tensor, we visualize the NP–RBC microstructure and carry out numerical experiments. Eventually, we construct empirical correlations for the complete NP diffusion tensor.

3.1. *Problem formulation*

The apparent diffusivity of NPs in unbounded blood flow under simple shear is determined by NP radius a_1, shear rate $\dot{\gamma}$ and haematocrit ϕ, with NP concentration in the dilute regime. The relevant dimensionless parameters (besides ϕ) primarily include the NP Péclet number,

$$Pe = \frac{\dot{\gamma} a_1^2}{D^B}, \tag{3.1}$$

expressing the ratio of shear-induced diffusion to Brownian diffusion, and the RBC capillary number,

$$Ca_G = \frac{\mu \dot{\gamma} a_2}{G}, \tag{3.2}$$

quantifying the competition between the fluid viscous stress and the membrane elastic stress. Here, μ is the dynamic viscosity of the suspending plasma, a_2 is the effective radius of the RBC and G is the elastic shear modulus of the RBC membrane; D^B is the Brownian diffusivity, which is determined by the Stokes–Einstein relation, $D^B = k_B T/6\pi\mu a_1$, where k_B is the Boltzmann constant and T is the absolute temperature. The NP Péclet number quantifies the severity of the NP Brownian effect, while the RBC capillary number determines the deformability of the RBC capsule.

To obtain appropriate scaling relations, we performed a large number of independent 3D simulations. Table 1 lists all the simulation parameters and the measured NP diffusivities. Wide ranges of shear rates ($10 \leqslant \dot{\gamma} \leqslant 10\,000\ \mathrm{s}^{-1}$) and haematocrits ($0 \leqslant \phi \leqslant 0.4$) with physiological relevance (Lipowsky 2005; Popel & Johnson 2005) are covered. Cases with $\dot{\gamma} = 10\,000\ \mathrm{s}^{-1}$ are to match certain vascular pathological conditions, e.g. the high shear induced thrombosis (Casa & Ku 2017). For discussions in this section, NP size is set to $2a_1 = 100$ nm. RBCs are assumed to be in a

https://doi.org/10.1017/jfm.2019.320 Published online by Cambridge University Press

$\dot{\gamma}$ (s^{-1})	ϕ	a_1/a_2	N^{RBC}	N^{NP}	Pe	Ca_G	D^{∞}_{xx}/D^B	D^{∞}_{yy}/D^B	D^{∞}_{zz}/D^B	D^{∞}_{xy}/D^B
10	0.0	0.017	0	5000	0.0066	0.0055	1.0	1.0	1.0	0.0
10	0.1	0.017	52	5000	0.0066	0.0055	1.4	1.1	1.1	0.05
10	0.2	0.017	104	5000	0.0066	0.0055	2.5	1.1	1.2	0.03
10	0.3	0.017	156	5000	0.0066	0.0055	2.6	1.1	1.3	0.05
10	0.4	0.017	208	5000	0.0066	0.0055	3.2	1.2	1.4	0.03
30	0.0	0.017	0	5000	0.020	0.017	1.0	1.0	1.0	0.0
30	0.1	0.017	52	5000	0.020	0.017	2.6	1.3	1.2	−0.1
30	0.2	0.017	104	5000	0.020	0.017	4.8	1.6	1.3	−0.2
30	0.3	0.017	156	5000	0.020	0.017	6.7	1.9	1.5	−0.2
30	0.4	0.017	208	5000	0.020	0.017	7.2	2.0	1.8	−0.4
100	0.0	0.017	0	5000	0.066	0.055	1.1	1.0	1.1	0.0
100	0.1	0.017	52	5000	0.066	0.055	7.3	1.9	1.6	−0.6
100	0.2	0.017	104	5000	0.066	0.055	14.5	2.9	2.0	−1.0
100	0.3	0.017	156	5000	0.066	0.055	18.9	3.7	3.1	−1.3
100	0.4	0.017	208	5000	0.066	0.055	29.2	4.1	3.8	−2.0
300	0.0	0.017	0	5000	0.198	0.165	1.0	1.0	1.0	0.0
300	0.1	0.017	52	5000	0.198	0.165	28.0	3.3	2.9	−2.2
300	0.2	0.017	104	5000	0.198	0.165	67.9	5.7	3.7	−4.3
300	0.3	0.017	156	5000	0.198	0.165	133.0	8.8	6.3	−7.6
300	0.4	0.017	208	5000	0.198	0.165	216.4	10.8	8.0	−9.1
1000	0.0	0.017	0	5000	0.66	0.55	1.0	1.0	1.0	0.0
1000	0.1	0.017	52	5000	0.66	0.55	73.8	7.0	8.1	−10.1
1000	0.2	0.017	104	5000	0.66	0.55	211.1	12.5	10.5	−14.9
1000	0.3	0.017	156	5000	0.66	0.55	674.2	19.1	16.1	−26.9
1000	0.4	0.017	208	5000	0.66	0.55	2095.9	23.2	18.8	−38.1
2000	0.0	0.017	0	5000	1.32	1.10	0.9	1.0	1.0	0.0
2000	0.1	0.017	52	5000	1.32	1.10	122.8	12.5	15.6	−19.9
2000	0.2	0.017	104	5000	1.32	1.10	350.0	20.7	21.5	−25.7
2000	0.3	0.017	156	5000	1.32	1.10	1379.3	29.6	26.3	−50.0
2000	0.4	0.017	208	5000	1.32	1.10	4150.3	36.6	29.4	−82.8
10 000	0.0	0.017	0	5000	6.60	5.52	1.1	1.0	1.0	0.0
10 000	0.1	0.017	52	5000	6.60	5.52	606.7	40.9	77.3	−73.1
10 000	0.2	0.017	104	5000	6.60	5.52	1363.7	44.9	86.4	−81.8
10 000	0.3	0.017	156	5000	6.60	5.52	2788.5	64.0	110.8	−138.0
10 000	0.4	0.017	208	5000	6.60	5.52	7575.6	80.4	120.3	−220.9

TABLE 1. Simulation data. Each case is simulated independently in an LB domain of size $128 \times 128 \times 80$ at specified Pe, Ca_G and ϕ. NP long-time diffusivities, D^{∞}_{xx}, D^{∞}_{yy}, D^{∞}_{zz} and D^{∞}_{xy}, normalized by the theoretical Brownian diffusivity, D^B, are listed for all cases. The unlisted off-diagonal diffusivities, D^{∞}_{xz} and D^{∞}_{yz}, are found to be negligible. The measured diffusivities have a standard deviation less than 5 %. RBCs have an effective radius of $a_2 =$ 2.9 μm. Brownian diffusivity is calculated by $D^B = k_B T/6\mu\pi a_1$ at temperature $T = 310$ K.

healthy state with an effective radius $a_2 = 2.9$ μm and a membrane shear modulus $G = 0.0063$ dyne cm^{-1}. The absolute temperature is set to $T = 37\,^{\circ}C$, at which the plasma has a viscosity $\mu = 1.2$ cP and a density $\rho = 1.0$ g cm^{-3}. The viscosity ratio of RBC cytoplasm to plasma is set to the physiological value $\lambda = 5.0$. The density

https://doi.org/10.1017/jfm.2019.320 Published online by Cambridge University Press

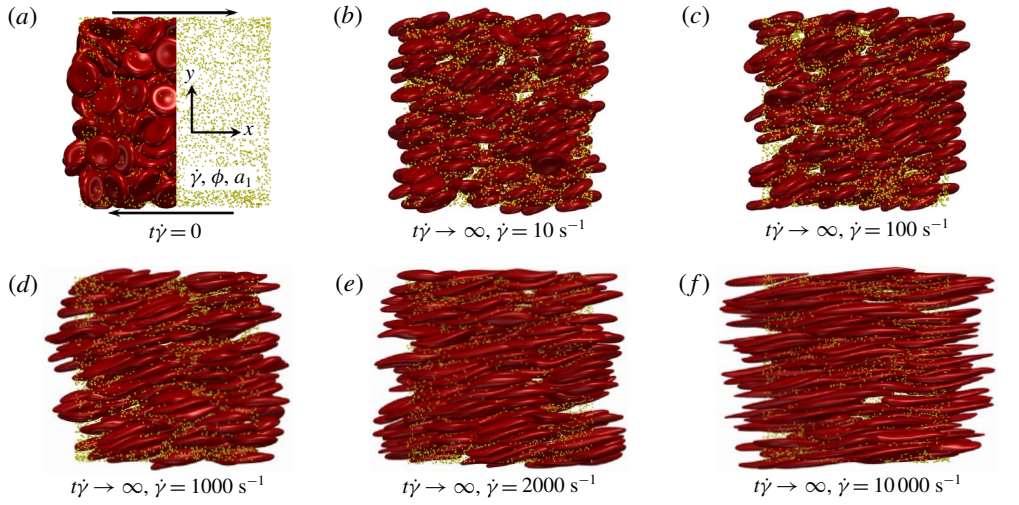


FIGURE 2. (Colour online) (*a*) The RBC–NP complex configuration at $t\dot{\gamma} = 0$. NPs and RBCs are randomly and uniformly mixed in an unbounded shear flow. RBCs are shown partially in the domain to visualize the NP phase. The athermal system is determined by shear rate $\dot{\gamma}$, haematocrit ϕ and NP radius a_1. (*b–f*) The RBC–NP complex configuration in the long-time scale regime under a shear rate of (*b*) $\dot{\gamma} = 10$, (*c*) 100, (*d*) 1000, (*e*) 2000 and (*f*) 10 000 s^{-1} with $\phi = 0.4$.

of cytoplasm is set to that of the plasma. The corresponding Pe and Ca_G lie in the ranges of $0.0066 \leqslant Pe \leqslant 6.60$ and $0.0055 \leqslant Ca_G \leqslant 5.52$, respectively. All simulations are formulated by matching the dimensionless group, i.e. ϕ, Pe and Ca_G.

Simulations are initiated by imposing steady shear flow on the uniformly, randomly mixed NPs and RBCs at specific shear rate in an LEbc computational domain, as shown in figure 2(*a*). The domain has a dimension of $128 \times 128 \times 80$ ($42.7\ \mu\mathrm{m} \times 42.7\ \mu\mathrm{m} \times 26.7\ \mu\mathrm{m}$) in longitudinal ($x$), velocity-gradient ($y$) and vorticity ($z$) directions, respectively. This LB domain size matches the highest resolution applied for the rheological characterization of cellular blood flow under shear by Reasor *et al.* (2013*a*). The selected LB grid resolution (300 nm per lattice unit) and the equilibrium RBC mesh size (1.5 lattice units per link length) have previously proven to be fine enough to capture both the single RBC dynamics (MacMeccan *et al.* 2009; Reasor *et al.* 2012) and the rheological properties of concentrated cellular blood flow (MacMeccan *et al.* 2009; Reasor *et al.* 2013*a*).

To obtain converged long-time diffusivity, sufficient strains ($t\dot{\gamma} \sim 1000$) and a large number of particles (5000 NPs and up to 208 RBCs) are employed for each simulation. The resolution of these simulations in terms of strain units and number of particles is at the high end compared to other numerical studies on particle diffusion in colloidal/non-colloidal suspensions (Foss & Brady 1999, 2000*b*; Sierou & Brady 2004; Yeo & Maxey 2010; Clausen *et al.* 2011; Gross *et al.* 2014; Mountrakis, Lorenz & Hoekstra 2016). As will be discussed in § 3.3.1, the selected resolution produces good agreement between the simulation results and the available experimental data.

Simulations are performed on the Intel Xeon Skylake nodes of the TACC (Texas Advanced Computing Center) Stampede-2 system where each node features 48 cores and a 2.1 GHz clock rate. For the case at $\phi = 0.4$ with 208 RBCs and 5000 NPs, each run takes ∼168 h on 32 cores (∼5376 core hours) to accomplish

https://doi.org/10.1017/jfm.2019.320 Published online by Cambridge University Press

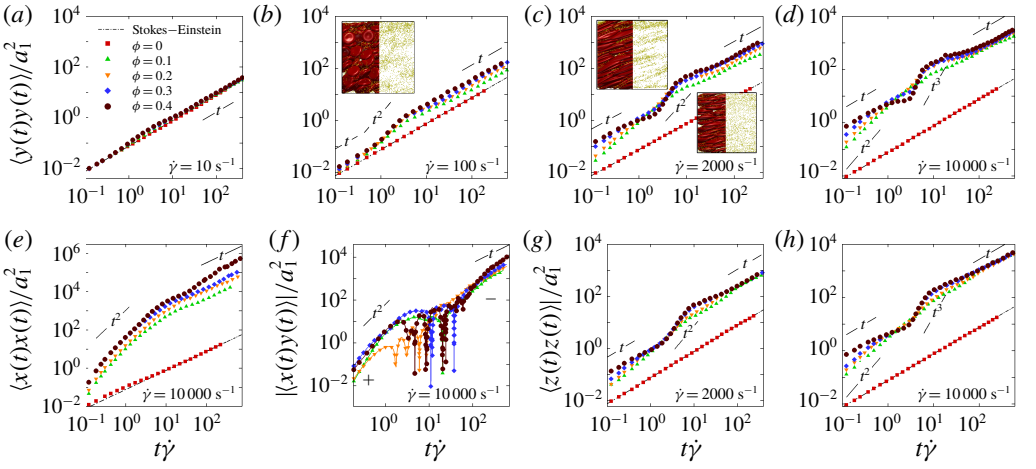


FIGURE 3. (Colour online) Normalized MSDs plotted against relative shear strains in logarithmic scale at various haematocrits for different shear rates. Panels (*a*)–(*d*) are concerned with evolutions of $\langle y(t)y(t)\rangle/a_1^2$; (*e*) and (*f*) depict evolutions of $\langle x(t)x(t)\rangle/a_1^2$ and $|\langle x(t)y(t)\rangle|/a_1^2$, respectively; (*g*) and (*h*) depict evolutions of $\langle z(t)z(t)\rangle/a_1^2$. The imposed shear rate is denoted on each plot. Inset of (*b*) shows the RBC–NP distribution at $t\dot{\gamma} \sim 1$ under $\dot{\gamma} = 100\ \mathrm{s}^{-1}$. Insets of (*c*) show the RBC–NP distribution at $t\dot{\gamma} \sim 1$ (upper) and $t\dot{\gamma} \sim 100$ (lower) under $\dot{\gamma} = 2000\ \mathrm{s}^{-1}$ and $\phi = 0.4$. An NP radius of $a_1 = 50$ nm is used for normalization. Cross-stream MSDs (*a–d*) and (*g*,*h*) are sampled starting from $t\dot{\gamma} = 0$ to capture the transient NP dispersive behaviour; streamwise and off-diagonal MSDs are sampled starting from $t\dot{\gamma} = 400$ to avoid the initial extra affine displacement induced by RBC elongation and orientation.

1000 strains ($t\dot{\gamma}$). The total computational cost for the 35 independent cases listed in table 1 is approximately 140 000 core hours.

3.2. *Temporal growth of NP transient mobility*

To understand the short-time dispersive characteristics of the NP phase, we examine the transient behaviour of NP mobility by tracking the temporal growth of NP MSDs. Cross-stream MSDs, $\langle y(t)y(t)\rangle/a_1^2$ and $\langle z(t)z(t)\rangle/a_1^2$, are sampled from the initial configuration ($t\dot{\gamma} = 0$) where NPs and RBCs are randomly and uniformly mixed, as shown in figure 2(*a*). Longitudinal and off-diagonal MSDs, $\langle x(t)x(t)\rangle/a_1^2$ and $\langle x(t)y(t)\rangle/a_1^2$, are sampled starting from a long-time configuration ($t\dot{\gamma} = 400$) to avoid any extra convective effect caused by the transient elongation and reorientation of RBCs. Such transient effects are found to introduce an extra affine displacement leading to $\sim t^3$ growth of MSDs and hence jeopardize the measurement of the long-time diffusivity in the x-relevant directions. The necessity of eliminating the affine effect for calculating streamwise diffusivities is elaborated by Foss & Brady (2000*b*) in the context of sheared colloidal suspensions.

Figure 3 plots the particle normalized MSD growth with respect to the relative strains sampled. At $\phi = 0$, all diagonal MSDs grow according to the Stokes–Einstein (SE) prediction with no dependence on shear rate, while the off-diagonal MSDs produce zero value (not shown). This is consistent with the isotropic nature of NP Brownian motion in a dilute and unbounded solution, and also serves as a verification of the MSD calculations. At $\phi > 0$, a deviation from the SE relation occurs in all

https://doi.org/10.1017/jfm.2019.320 Published online by Cambridge University Press

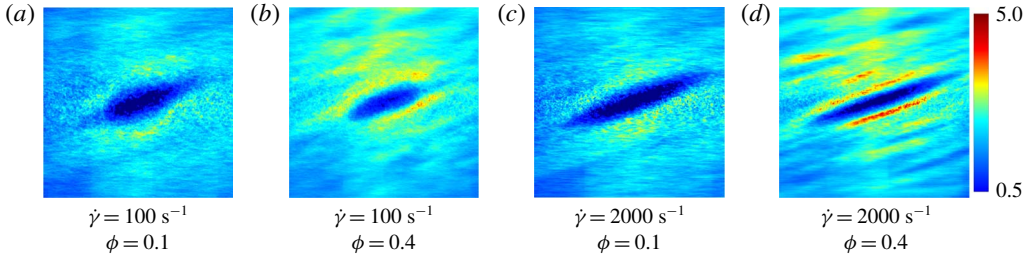


FIGURE 4. (Colour online) RBC–NP partial pair distribution function, $g_{21}(\boldsymbol{r})$, projected on the xy plane under various haemorheological conditions and averaged in the strain range of $t\dot{\gamma} = 1$–3.

diagonal MSDs as a result of NP–RBC interactions. At $\dot{\gamma} = 10\ \mathrm{s}^{-1}$, only a slight deviation from the SE relation is observed given the dominance of Brownian diffusion; see figure 3(*a*).

The transient deviation of NP mobility from the SE relation can be further interrogated through the evolution of cross-stream MSDs, as depicted in figure 3(*a–d*, *g–h*). In the short-time regime ($t\dot{\gamma} \ll 1$), a linear growth of MSD ($\sim t$) is observed particularly under low-shear-rate (e.g. $\dot{\gamma} \leqslant 100\ \mathrm{s}^{-1}$) or high-shear-rate and high-hematocrit (e.g. $\dot{\gamma} \geqslant 2000\ \mathrm{s}^{-1}$ and $\phi = 0.4$) conditions, as shown in figure 3(*b*) and (*c*), respectively. The short-time linear growth of MSD suggests a short-time diffusive mechanism. Since the short-time linear growth of MSD always occurs before the ballistic regime ($\sim t^2$) where RBC–NP collisions start to occur, such a short-time diffusive driver should logically be the Brownian effect. Therefore, the initial linear MSD growth at low shear rates (with $\phi = 0 \sim 0.4$) or high shear rates (with $\phi = 0.4$) can be explained by the Brownian diffusive time scale being much shorter than the RBC–NP collision time scale under such haemorheological conditions. However, under high shear rate (e.g. $\dot{\gamma} \geqslant 2000\ \mathrm{s}^{-1}$), the diffusive behaviour ($\sim t$) turns to ballistic ($\sim t^2$) as ϕ increases to 0.4; see figure 3(*c*,*d*,*g*,*h*). This is probably due to the high convective (high-shear-rate) and low inertial (low-haematocrit) effects that reduce the RBC–NP collision time scale to be comparable to the Brownian diffusion time scale. As a result, the Brownian diffusion of NP is overwhelmed by the ballistic behaviour caused by insufficient RBC–NP collisions.

In the intermediate-time regime, $t\dot{\gamma} = O(1)$–$O(10)$, anomalous dispersive behaviour is observed as RBCs start to elongate and rotate to be aligned with the streamwise direction due to shear. For cases at high shear rates ($\dot{\gamma} \geqslant 2000\ \mathrm{s}^{-1}$) and high haematocrit ($\phi = 0.4$), we observe a sublinear growth of MSD, representing a temporary hindrance of the NP mobility. This hindrance effect is caused by a string-ordered microstructure of NP in the shearing plane accompanied by the elongation and alignment of RBCs; see the contrast between the upper inset of figure 3(*c*) and the inset of figure 3(*b*) (see also supplementary movie 2, available at https://doi.org/10.1017/jfm.2019.320). Such string-ordered NP distribution can be better visualized by plotting the RBC–NP partial pair distribution function (PPDF), $g_{21}(\boldsymbol{r})$, projected on the xy plane (the computing procedure of PPDF in the short-time regime is discussed in appendix B). As shown in figure 4, $g_{21}(\boldsymbol{r})$ in the xy plane exhibits streaks showing an intensified distribution particularly near the RBC surface under high shear rate and high haematocrit, while in contrast no significant string structure is found in low shear rate ($\dot{\gamma} \leqslant 100\ \mathrm{s}^{-1}$) (see supplementary movie 1) or/and low haematocrit ($\phi = 0.1$) cases, as shown in figure 4(*a–c*). Note that a suspension

https://doi.org/10.1017/jfm.2019.320 Published online by Cambridge University Press

string-like structure often occurs in sheared monodisperse colloidal suspensions at equilibrium as a consequence of the absence of interparticle lubrication interactions at high concentration (Xue & Grest 1990; Foss & Brady 2000*b*) or the presence of long-range repulsive forces at low concentration (Kumar & Higdon 2010). However, in the current case, ordering of NPs occurs at a non-equilibrium state that involves the change of the RBC suspension structure from a uniformly distributed and randomly oriented configuration to a streamwise-aligned and elongated configuration under high shear and high haematocrit. The sublinear growth of MSD is followed by a super-ballistic behaviour ($\sim t^3$) at high shear rate ($\dot{\gamma} = 10000\ \mathrm{s}^{-1}$), which might be associated with the large jump of NPs between strings when the NP phase gradually evolves from the string-like structure towards the more uniform structure featuring in the long-time diffusive regime.

In the long-time regime ($t\dot{\gamma} > 100$), MSD reaches the second linear growth stage ($\sim t$), where RESID becomes the dominate diffusive mechanism leading to a uniform distribution of NP (see lower inset of figure 3*c*). Such a three-stage (diffusive/super-ballistic/diffusive) anomalous dispersion behaviour has previously been reported in the dispersion of Brownian particles subjected to external forces (Siegle, Goychuk & Hanggi 2010). Here, we show that such dispersive anomalies also occur in a sheared NP–RBC bidisperse suspension, where the anomalous NP dispersion is, however, driven by an internal shear-induced mechanism, i.e. the elongation and the alignment of the concentrated RBCs along the streamwise direction under high shear. Such transient shear-induced morphological adaptation of RBCs contributes to extra mobility of the NP phase, seemingly playing a role of external forces exerted on the NP phase.

Figures 3(*e*,*f*) depict the longitudinal and off-diagonal MSD evolution at $\dot{\gamma} = 10\,000\ \mathrm{s}^{-1}$. Results for lower shear rate show similar MSD behaviours and are not presented for discussion. Because the initial transient regime is neglected, the longitudinal and off-diagonal MSDs yield classical ballistic–diffusive transitions similar to the dispersive behaviour of rigid-particle suspensions under shear (Foss & Brady 1999; Clausen *et al.* 2011). The off-diagonal MSD under high shear starts with positive values during the ballistic regime, exhibits a cross-over transition involving a change of sign, and eventually maintains negative values in the diffusive regime. Absolute values are shown for the off-diagonal MSDs with the sign at certain temporal stage denoted in figure 3(*f*). The change of sign from positive (+) to negative (−) is a hallmark of the dominant NP migration direction shifted from along the extensional axes (first and third quadrants) to along the compressive axes (second and fourth quadrants) of the flow, as also observed in sheared colloidal suspensions (Foss & Brady 1999).

3.3. *Haemorheological dependence of NP long-time diffusivity*

In this section, we focus on examining the NP long-time diffusive behaviour. The NP long-time diffusivities are evaluated in the long-time regime (after 100 strain units) and listed in table 1. Experimental statistics from various sources (Grabowski *et al.* 1972; Antonini *et al.* 1978; Diller *et al.* 1980; Wang & Keller 1985) are selected for comparison to gain credibility of the simulation results. Given the distinct time scales associated with the Brownian ($\tau_B \sim 10^{-4}$ s) and the long-time RBC-enhanced diffusion ($\tau_R \sim 100/\dot{\gamma}$) phenomenon, the coupling of BD and RESID follows a simple superposition, $D^{\infty}_{ij} = D^{R}_{ij} + D^{B}\delta_{ij}$, as confirmed in previous studies (e.g. Liu *et al.* 2018), where D^{R}_{ij} denotes the RESID. Since D^{B} at infinite dilution follows the SE relation with negligible dependence on flow conditions, the haemorheological response of D^{∞}_{ij} is essentially determined by D^{R}_{ij}.

https://doi.org/10.1017/jfm.2019.320 Published online by Cambridge University Press

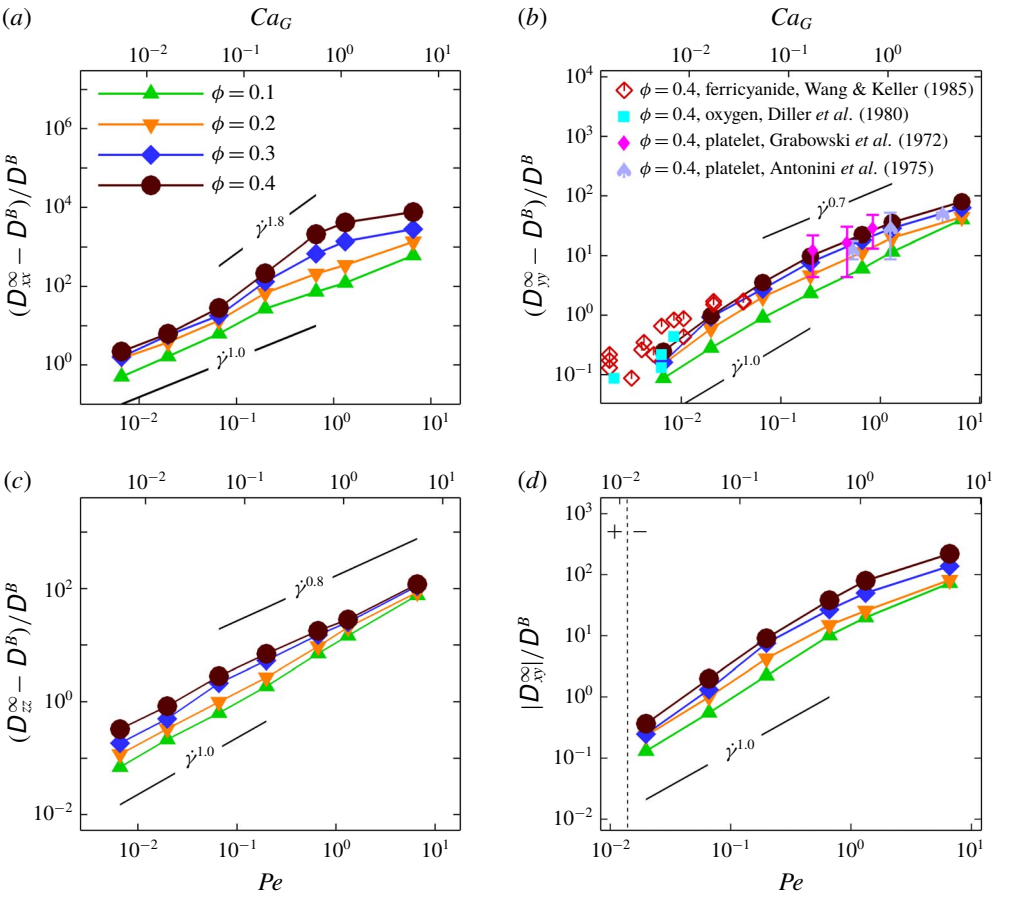


FIGURE 5. (Colour online) Normalized particle long-time RESID in (*a*) *xx*, (*b*) *yy*, (*c*) *zz* and (*d*) *xy* directions against normalized shear rate (*Pe* or Ca_G) in a log–log scale. Each curve at specific ϕ forms by connecting $\hat{D}^R_{ij}$ data at shear rate $\dot{\gamma} = 10$, 30, 100, 300, 1000, 2000 and 10 000 s^{-1}, from left to right; $\hat{D}^R_{xy}$ at $\dot{\gamma} = 10\ \mathrm{s}^{-1}$ is not shown for scaling purpose due to its small magnitude. Experimental results for RBC enhanced solute (Diller, Mikic & Drinker 1980; Wang & Keller 1985) and platelet (Grabowski, Friedman & Leonard 1972; Antonini *et al.* 1978) diffusivity in the velocity-gradient (*yy*) direction are plotted for comparison. NPs of size $2a_1 = 100$ nm yield $D^B = 3.78\ \mu\mathrm{m}^2\ \mathrm{s}^{-1}$.

3.3.1. *Shear-rate dependence*

Figure 5 plots the normalized RESID, $\hat{D}^R_{ij} = D^{\infty}_{ij}/D^B - \delta_{ij}$, against normalized shear rate, *Pe* (or Ca_G). To first validate the simulation results, experimental results of solute or cell velocity-gradient (*yy*) diffusivity in sheared human or animal blood are selected for comparison; see figure 5(*b*). Wang & Keller (1985) measured the augmentation of ferricyanide solute diffusivity in both bovine and human RBC suspensions using a rotating Couette flow device. Diller *et al.* (1980) measured the enhanced radial diffusivity of oxygen solute in human blood using a tube oxygenator device. Grabowski *et al.* (1972) calculated the platelet velocity-gradient diffusivity in cavine (guinea pig) blood flowing through a channel by measuring the platelet rate

https://doi.org/10.1017/jfm.2019.320 Published online by Cambridge University Press

of adhesion/deposition to a foreign surface attached to the flow chamber. A similar experiment was later conducted by Antonini *et al.* (1978) to measure the platelet radial diffusivity in human blood. These measured diffusivities in 40 % haematocrit normalized based on our notation compares favourably with the calculated $\hat{D}^R_{yy}$ at $\phi = 0.4$ based on the simulation, as shown in figure 5(*b*).

Depending on the level of shear rate imposed at various haematocrits, the diffusion tensor of NP in sheared blood shows different shear-rate dependence. At low shear rates ($\dot{\gamma} \leqslant 100$), all RESID terms exhibit a linear dependence on shear rate ($\sim\dot{\gamma}$), matching the linear $\dot{\gamma}$ scaling of shear-induced diffusivity in rigid-particle suspensions (Foss & Brady 1999; Sierou & Brady 2004). This is also consistent with the insignificant RBC morphological changes at $\dot{\gamma} \leqslant 100\ \mathrm{s}^{-1}$, as shown in figure 2(*a–c*).

At intermediate shear rates ($100 \leqslant \dot{\gamma} \leqslant 2000$), significant streamwise elongation of RBCs occurs with increasing shear rate; see figure 2(*c–e*). As a result, nonlinear $\dot{\gamma}$ scaling is observed in all diagonal RESID terms. Specifically, cross-stream diffusivities, $\hat{D}^R_{yy}$ and $\hat{D}^R_{zz}$, show sublinear scales ($\sim\dot{\gamma}^m$, $m = 0.7$–0.8), while streamwise diffusivity, $\hat{D}^R_{xx}$, exhibits superlinear scales ($\sim\dot{\gamma}^n$, $n = 1$–1.8). In contrast to the nonlinear scaling in diagonal diffusivities, $\hat{D}^R_{xy}$ maintains largely a linear scale at the intermediate shear-rate regime, as shown in figure 5(*d*). It is also noted that such nonlinear shear-rate scaling in diagonal RESID terms is most prominent at intermediate to high haematocrit ($\phi > 0.1$), which implies that RBC deformability plays a less important role in altering the RESID shear dependence at low haematocrits. This observation is consistent with the results of shear-augmented solute diffusivity in model-RBC suspensions at various RBC deformability reported by Wang & Keller (1985), where they found changing RBC deformability barely affects the augmentation at a particle volume concentration of 0.1 or less. Wang & Keller (1985) also find a sublinear scaling of $\sim\dot{\gamma}^\beta$ ($0.67 \leqslant \beta \leqslant 0.89$) for the solute diffusivity in velocity-gradient directions, while our simulations observe an exponent of $\beta = 0.7$.

At high shear rates ($\dot{\gamma} \geqslant 2000$) and intermediate to high haematocrit ($\phi > 0.1$), all RESID terms except $\hat{D}^R_{zz}$ exhibit reduced shear-rate dependence compared to the intermediate shear-rate regime. In the velocity-gradient (y) direction, the hindrance of diffusion is due to the fact that the concentrated RBCs become more aligned and elongated with flow such that RBCs act as obstacles against the NP cross-stream diffusion in the y direction; see figure 2(*f*). Such an effect, however, shows less hindrance on $\hat{D}^R_{zz}$, as it does not forbid the NP migration in the vorticity (z) direction. In the streamwise (x) direction, the reduction of the shear dependence of $\hat{D}^R_{xx}$ is likely to be associated with the saturation of the RBC elongation. Owing to the compound effects in both x and y directions, the off-diagonal diffusivity, $\hat{D}^R_{xy}$, also exhibits a certain reduction of the shear-rate dependence.

3.3.2. *Haematocrit dependence*

Figure 6 displays the same data as figure 5 but plotted against ϕ to show the haematocrit dependence of RESID at different shear rate. At low shear rates ($\dot{\gamma} \leqslant 100$), all diffusion terms manifest a linear ϕ scaling. Note that a linear concentration dependence of particle self-diffusivity has been observed in sheared monodisperse suspensions in the presence of surface roughness (Da Cunha & Hinch 1996) or residual Brownian motion (Brady & Morris 1997), which causes the two-body interaction to be irreversible and hence give rise to a diffusive behaviour. Since the shear-induced diffusion of NP is driven by NP–RBC interaction, it is likely that the

https://doi.org/10.1017/jfm.2019.320 Published online by Cambridge University Press

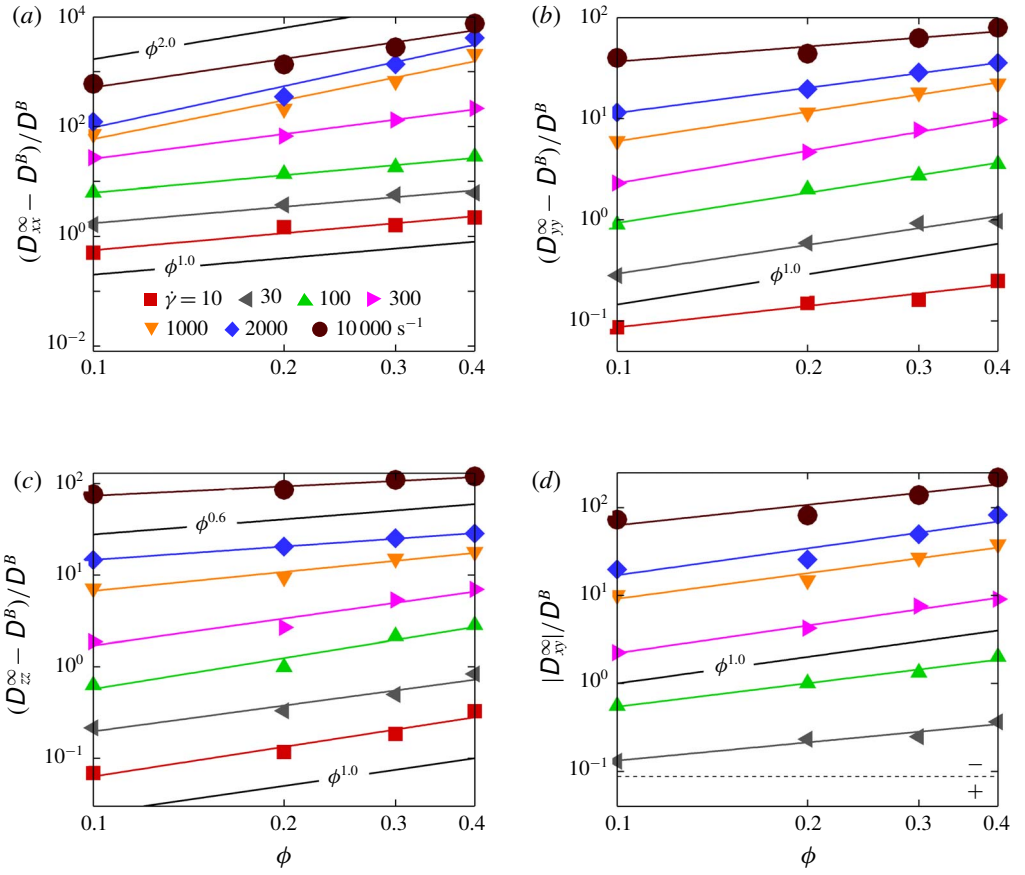


FIGURE 6. (Colour online) Normalized particle long-time RESID in (*a*) *xx*, (*b*) *yy*, (*c*) *zz* and (*d*) *xy* directions against haematocrit under different shear rate in logarithm scale. Lines are the best power-law fits to the data points at specific $\dot{\gamma}$. The $\hat{D}^R_{xy}$ value at $\dot{\gamma} = 10$ s^{-1} (not shown) is positive with negligible magnitude compared to other diffusion terms. NPs of size $2a_1 = 100$ nm yield $D^B = 3.78$ μm^2 s^{-1}.

ϕ scaling of the NP diffusion tensor results from the irreversible two-body interaction between NP and RBC induced by the RBC membrane roughness/flexibility and the NP Brownian effect. The off-diagonal diffusivity $\hat{D}^R_{xy}$ is found to be positive (+) at very low shear rate ($\dot{\gamma} \leqslant 10$ s^{-1}) and otherwise negative (−). The change-of-sign behaviour of the off-diagonal diffusivity designates the dominant displacement direction of NP changing from along the extensional axes to along the compressive axes of the flow as shear rate increases. A similar observation has been reported in sheared monodisperse colloidal suspensions (Foss & Brady 1999).

As shear rate grows above 100 s^{-1}, various ϕ scaling arises in different RESID components. The $\hat{D}^R_{xx}$ component exhibits a quadratic ϕ scaling ($\sim\phi^2$), which suggests that in the *x* direction additional effects exist to drive the NP diffusive motion besides the irreversible pairwise interactions. The $\hat{D}^R_{yy}$ and $\hat{D}^R_{xy}$ components scale linearly with ϕ, suggesting that the irreversible pairwise interaction remains the dominant diffusive

https://doi.org/10.1017/jfm.2019.320 Published online by Cambridge University Press

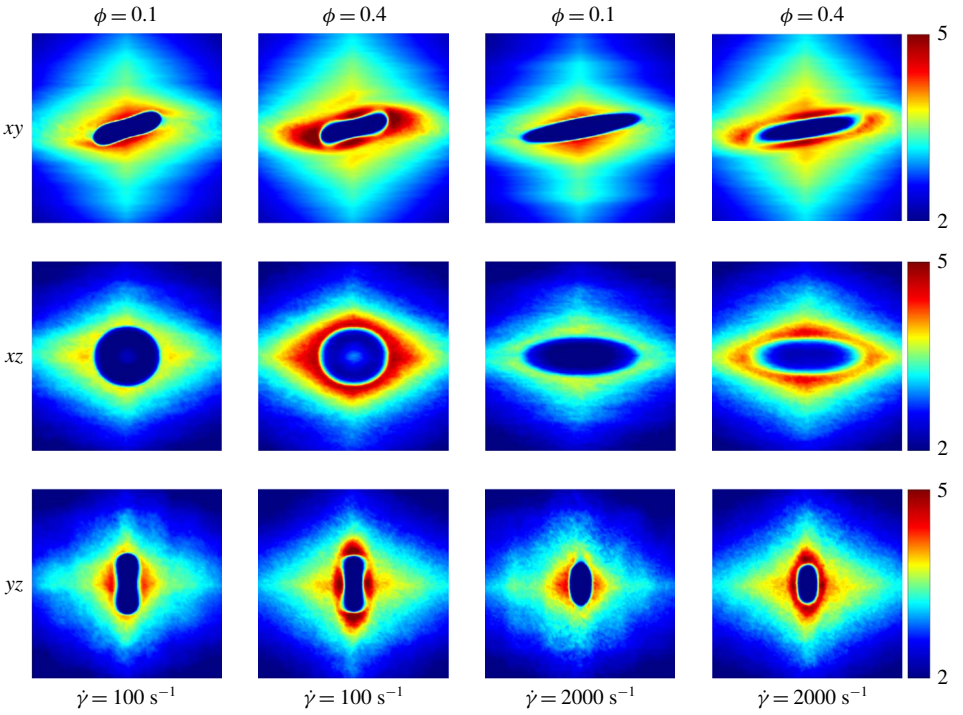


FIGURE 7. (Colour online) RBC–NP partial pair distribution function, $g_{21}(\boldsymbol{r})$, projected onto the xy, xz and yz planes in the long-time regime under various haemorheological conditions, where the PPDF contour has the horizontal edge aligned with the first axis (e.g. xy PPDF contour has the horizontal edge aligned with the x axis). The edge length of the sampling box for computing $g_{21}(\boldsymbol{r})$ is three times the maximum diameter of the undeformed RBC.

mechanism. The $\hat{D}^R_{zz}$ component exhibits a transition from linear to sublinear ϕ scale ($\sim\phi^{0.6}$). The mostly linear ϕ scale in $\hat{D}^R_{yy}$ observed in the current numerical study is consistent with the experimental observation in Wang & Keller (1985), where they show that the solute diffusivity in the velocity-gradient (y) direction is augmented by approximately threefold when the particle concentration increases from 0.1 to 0.31. Since suspension viscosity typically increases with particle concentration (Foss & Brady 2000*b*), the enhancement of solute (e.g. NP) diffusivity at increased ϕ indicates that the RESID is due to the RBC–NP interaction rather than the secondary flow effect (Wang & Keller 1985).

3.4. *Microstructure*

The rheological properties of particle suspensions are often determined by the mechanistic phenomenon occurring on the particle length scales. To elucidate the physical mechanisms that govern the haemorheological scaling behaviours of the NP diffusion tensor observed in § 3.3, the RBC–NP PPDF, $g_{21}(\boldsymbol{r})$, in the long-time regime is plotted to visualize the configurational microstructure of the RBC–NP bidisperse suspension under various haematocrits and shear rates. The techniques used to compute and project $g_{21}(\boldsymbol{r})$ are discussed in detail in appendix B.

Figure 7 presents a matrix of $g_{21}(\boldsymbol{r})$ projections onto the velocity–velocity gradient (xy) plane, the velocity–vorticity (xz) plane and the velocity gradient–vorticity (yz)

https://doi.org/10.1017/jfm.2019.320 Published online by Cambridge University Press

plane under two shear rates ($\dot{\gamma} = 100$ or 2000 s^{-1}) and two haematocrits ($\phi = 0.1$ or 0.4). In general, all PPDFs feature a large-scale rhombus shape as opposed to the typical circular shape commonly observed in rigid-sphere-particle suspensions (Foss & Brady 2000*a*; Wang & Brady 2016; Pednekar, Chun & Morris 2018). This can be attributed to the disk shape of RBC that causes geometry-specific anisotropy of the microstructure. The average RBC shapes under various haemorheological conditions, as shown in the central low-intensity region of the PPDF contours, are nicely captured through the PPDF sampling procedure. All PPDFs considered in the xy plane show more intensified distribution (i.e. higher probability of RBC–NP interaction) near the RBC disk surfaces, of which the surface normal directions are more aligned with the compressive axes (in second and fourth quadrants) in accordance with the negative values of $\hat{D}^R_{xy}$. In the xz and yz plane, the PPDF distribution tends to be symmetric about the principal axes (x, y or z), which explains the zero values of the xz and yz diffusivities.

As the haemorheological condition changes, the detailed configuration of the PPDF within the rhombus structure also varies. At low haematocrit ($\phi = 0.1$), the xy PPDF shows fore–aft low intensity similar to rigid-particle suspensions (Kumar & Higdon 2011). However, the break of the fore–aft symmetry, being different from the rigid-particle suspensions, seems to be related to the RBC orientation aligned with the extensional flow axes that is further caused by the tank-treading motion of the RBC membrane (Reasor *et al.* 2013*a*). As the haematocrit increases to $\phi = 0.4$, the overall PPDF around the RBC becomes more intensified, meaning the local NP concentration near the RBC surface increases. More interestingly, the fore–aft low PPDF region observed under low haematocrit gets intensified substantially. The change of the NP microstructure with increased haematocrit can be explained by smaller inter-cell separation and hence NP getting squeezed in a smaller inter-cell region. At low shear rate ($\dot{\gamma} = 100$ s^{-1}), RBC shows a close-to-equilibrium biconcave shape. Increasing the shear rate to $\dot{\gamma} = 2000$ s^{-1} results in a significant elongation of the average RBC shape in the flow (x) direction accompanied by certain contraction in the velocity-gradient (y) and vorticity (z) directions.

The above configurational changes of $g_{21}(\boldsymbol{r})$ under various shear rates and haematocrits provide possible mechanistic explanations for the nonlinear ϕ dependence observed at high shear rates, as discussed in § 3.3.2. The quadratic dependence of $\hat{D}^R_{xx}$ ($\sim\phi^2$), shown in figure 6(*a*), is probably due to the occurrence of three-body RBC–NP interactions in the longitudinal (x) direction caused by the compound effect of the elevated NP concentration at the RBC fore–aft surface and the elongation of the RBC in the x direction. The reduced ϕ dependence in $\hat{D}^R_{zz}$ at high shear rate, as shown in figure 6(*c*), can be attributed to the relatively large contraction of the RBC in the vorticity direction, which reduces the effective ϕ in the z direction. The lesser reduction of the ϕ dependence in the y direction, as shown in figure 6(*c*), is due to the y direction contraction of RBC under shear being less significant than that in the z direction, as clearly indicated in the PPDF contours.

3.5. *Role of RBC deformability*

The above PPDF analysis shows prominent RBC morphological change with elevated shear rate, which suggests that RBC deformability may play an important role in causing the nonlinear $\dot{\gamma}$ dependence of the NP diffusion tensor. In this section, we perform numerical experiments to further quantitatively explain the nonlinear $\dot{\gamma}$ scaling of RESID in the intermediate-shear-rate regime ($100 \leqslant \dot{\gamma} \leqslant 2000$ s^{-1}),

https://doi.org/10.1017/jfm.2019.320 Published online by Cambridge University Press

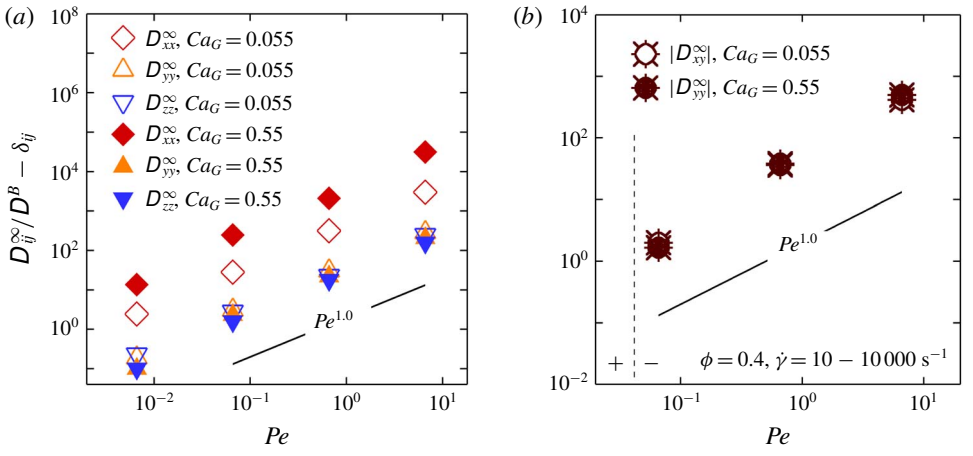


FIGURE 8. (Colour online) The Pe dependence of the (a) diagonal and (b) off-diagonal RESID terms at fixed capillary number (by rescaling G) with $\phi = 0.4$. Two RBC capillary numbers, $Ca_G = 0.55$ and 0.055, are considered to see the isolated effect of changing RBC deformability (Ca_G) or adjusting the inertial effect (Pe).

$\dot{\gamma}$ (s^{-1})	ϕ	a_1/a_2	N^{RBC}	N^{NP}	Pe	Ca_G	D_{xx}^{∞}/D^B	D_{yy}^{∞}/D^B	D_{zz}^{∞}/D^B	D_{xy}^{∞}/D^B
10	0.4	0.017	208	5000	0.0066	0.055	3.4	1.2	1.2	0.06
100	0.4	0.017	208	5000	0.066	0.055	29.2	4.1	3.8	−2.0
1000	0.4	0.017	208	5000	0.66	0.055	317.6	31.6	23.8	−36.1
10 000	0.4	0.017	208	5000	6.60	0.055	2999.8	286.9	248.6	−416.0
10	0.4	0.017	208	5000	0.0066	0.55	14.6	1.1	1.1	0.35
100	0.4	0.017	208	5000	0.066	0.55	247.6	3.3	2.6	−1.66
1000	0.4	0.017	208	5000	0.66	0.55	2095.9	23.2	18.8	−38.1
10 000	0.4	0.017	208	5000	6.60	0.55	31698.3	209.0	158.3	−499.3

TABLE 2. Simulation data for numerical experiments concerning the isolated RBC deformation effect in NP–RBC suspensions. The RBC membrane shear modulus, G, is rescaled to numerically match specific Ca_G while changing shear rate. Here, the NP size is fixed to $2a_1 = 100$ nm; RBC has an effective radius of $a_2 = 2.9$ μm. Brownian diffusivity is calculated by $D^B = k_B T/6\mu\pi a_1$ at a temperature of $T = 310$ K.

as observed in § 3.3.1. Changing shear rate alters both the fluid inertia and RBC deformability, quantified by Pe and Ca_G, respectively. To interrogate the isolated effect of RBC deformability (Ca_G), we fix Ca_G by scaling up G while increasing Pe (through increasing $\dot{\gamma}$). Two capillary numbers, $Ca_G = 0.055$ and 0.55, are considered corresponding to the Ca_G regime where the nonlinear shear-rate dependence of RESID occurs. For these simulations, we select a fixed haematocrit of $\phi = 0.4$ and an NP size of $2a_1 = 100$ nm. Table 2 lists all parameters and the NP diffusivity values for the cases tested.

As presented in figure 8(a,b), instead of exhibiting nonlinear Pe scaling as observed in § 3.3.1, all RESID components show a linear dependence on Pe at fixed RBC capillary number of $Ca_G = 0.55$ or 0.055 across the wide range of shear rates. This recovers the linear Pe dependence of solute/self-diffusivity in sheared rigid-particle

https://doi.org/10.1017/jfm.2019.320 Published online by Cambridge University Press

suspensions (Zydney & Colton 1988; Foss & Brady 1999; Sierou & Brady 2004) since we intentionally fix the RBC deformation (Ca_G) while adjusting Pe.

Moreover, an increase of Ca_G (from 0.055 to 0.55) leads to an increase of $\hat{D}^R_{xx}$ but a decrease of $\hat{D}^R_{yy}$ and $\hat{D}^R_{zz}$, as shown in figure 8(*a*). These results are direct evidence indicating that the nonlinear shear-rate scaling of the diagonal RESID terms observed in § 3.3.1 is due to the variation of RBC deformability (Ca_G) induced by changing shear rate at fixed G. More specifically, the increase of Ca_G with increasing shear rate at $100 < \dot{\gamma} < 2000\ \mathrm{s}^{-1}$ under fixed G leads to the superlinear shear-rate dependence of longitudinal diffusivity and meanwhile the sublinear dependence of cross-stream diffusivities. In figure 8(*b*), the off-diagonal diffusivity shows insignificant change at different Ca_G, consistent with its mostly linear shear-rate dependence shown in figure 5(*d*).

3.6. *Relevant length scale*

Although the shear adaptation of the RBC deformability is shown to be responsible for the nonlinear shear-rate dependence of the RESID, it is still unclear in what way it alters the RESID. In this section, we further identify the characteristic length scale relevant to the RESID to gain a more in-depth understanding of this nonlinear phenomenon.

In a series of experiments measuring the particle diffusivity in a concentrated non-colloidal suspension, Breedveld *et al.* (1998) show that the ratio of the diffusivity of fluid tracers to the self-diffusivity of non-colloidal particles is close to unity. Through DNS of the cellular blood flow in a microchannel, Zhao *et al.* (2012) show that the cross-stream diffusivity of platelets ($\sim$2 μm) in blood exhibits similar magnitude to that of passive tracers. These findings imply that the shear-induced diffusivity is insensitive to the size of the scarce (in terms of volume fraction) small particles. Following these results, we hypothesize that RESID is insensitive to the size of NPs. Moreover, the characteristic length scale associated with the RESID should be the size of RBCs. To confirm this hypothesis, we evaluate the RESID at fixed haemorheological condition with various NP size. The NP size is kept in submicrometre scale such that the NP–RBC size ratio satisfies $a_1/a_2 \ll 1$. The volume fraction of the NP phase is kept below 0.32 % to satisfy the dilute condition. The set-up and measured diffusivities are listed in table 3.

In figure 9(*a*), we plot the RESID versus Pe at $\dot{\gamma} = 1000\ \mathrm{s}^{-1}$ and $\phi = 0.2$. Here, Pe is adjusted by NP size in the range of $50 \leqslant 2a_1 \leqslant 800$ nm. A sublinear $\hat{D}^R_{ij}$–Pe relationship is observed for all diffusion coefficients. Figure 9(*b*) further plots the same data as figure 9(*a*), but with Pe rescaled by the NP–RBC size ratio as

$$\widetilde{Pe} = Pe\left(\frac{a_2}{a_1}\right)^2 = \frac{\dot{\gamma}a_2^2}{D^B}. \tag{3.3}$$

This simple rescaling leads to a strong linear relationship between all RESID terms and the rescaled Péclet number, $\widetilde{Pe}$. Moreover, the observed linear relationship, $(D^\infty_{ij}/D^B - \delta_{ij}) \sim O(\widetilde{Pe})$, can be deduced to show that $D^R_{ij} \sim O(\dot{\gamma}a_2^2)$, which indicates that the dimensional RESID is indeed insensitive to the NP size within the range of NP sizes considered in the current study. This also suggests that NPs at submicrometre size play a secondary role in affecting the NP apparent diffusivity primarily through altering BD.

https://doi.org/10.1017/jfm.2019.320 Published online by Cambridge University Press

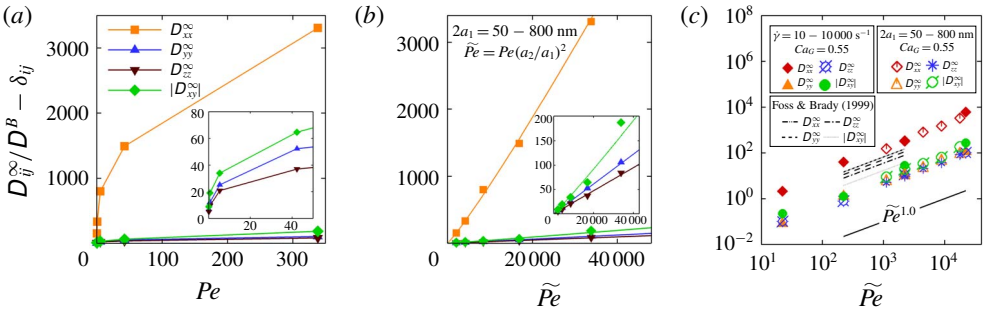


FIGURE 9. (Colour online) RESID plotted against (*a*) Péclet number Pe and (*b*) the rescaled Péclet number $\widetilde{Pe}$, at $\dot{\gamma} = 1000\ \mathrm{s}^{-1}$ and $\phi = 0.2$ in logarithmic scales. Both Pe and $\widetilde{Pe}$ are adjusted with NP size in the range of $2a_1 = 50$–800 nm. (*c*) Linear dependence of RESID on $\widetilde{Pe}$ at fixed $Ca_G = 0.55$ and $\phi = 0.2$; $\widetilde{Pe}$ is adjusted by shear rate (with $2a_1 = 100$ nm) or NP size (with $\dot{\gamma} = 1000\ \mathrm{s}^{-1}$). The diffusion tensor in monodisperse colloidal suspensions (Foss & Brady 1999) is also plotted for comparison, where $\widetilde{Pe}$ degrades to Pe.

$\dot{\gamma}$ (s^{-1})	ϕ	a_1/a_2	N^{RBC}	N^{NP}	Pe	Ca_G	D^∞_{xx}/D^B	D^∞_{yy}/D^B	D^∞_{zz}/D^B	D^∞_{xy}/D^B
1000	0.2	0.017	104	5000	0.66	0.55	211.1	12.5	10.5	−14.9
1000	0.2	0.034	104	5000	5.28	0.55	801.1	26.3	21.9	−34.1
1000	0.2	0.069	104	5000	42.28	0.55	1491.9	53.3	38.1	−64.7
1000	0.2	0.14	104	500	338.23	0.55	3309.1	106.9	84.9	−186.8
10	0.2	0.017	104	5000	0.0066	0.55	3.1	1.0	1.1	0.2
100	0.2	0.017	104	5000	0.066	0.55	40.9	2.3	1.8	−1.3
10 000	0.2	0.017	104	5000	6.60	0.55	6109.4	113.0	102.2	−270.5

TABLE 3. Simulation data for numerical experiments concerning the relevant length scale in NP–RBC suspensions. NP size is varied in the range of $2a_1 = 50$–800 nm. RBC has an effective radius of $a_2 = 2.9$ μm. Brownian diffusivity is calculated by $D^B = k_B T/6\mu\pi a_1$ at temperature $T = 310$ K. For the 800 nm case, the number of NPs is set to 500 to satisfy the dilute condition for the NP volume fraction. The last three cases are performed with adjusted G to fix Ca_G.

To further justify the universality of the rescaled Péclet number, $\widetilde{Pe}$, i.e. whether the RBC size is the reasonable length scale associated with RBC-enhanced diffusion or not, we plot RESID against $\widetilde{Pe}$ at $Ca_G = 0.55$ and $\phi = 0.2$, with $\widetilde{Pe}$ adjusted by either shear rate or NP size. As shown in figure 9(*c*), the data points for a particular RESID coefficient are found to be well aligned on the same linear $\widetilde{Pe}$ scaling line. This directly confirms that the RBC size is the characteristic length scale governing the RBC-enhanced diffusion, and $\widetilde{Pe}$ is a more general non-dimensional term quantifying the RESID.

Identifying RBC size as the RESID length scale helps in further understanding the nonlinear shear-rate dependence of the RESID. In figure 10, we present snapshots of RBC and NP distribution and morphology in the mid-cross-stream cross-sectional plane. As shown in figure 10, the x direction elongation of RBCs under high shear causes a contraction of RBCs in the yz plane, which causes a reduction of the average

https://doi.org/10.1017/jfm.2019.320 Published online by Cambridge University Press

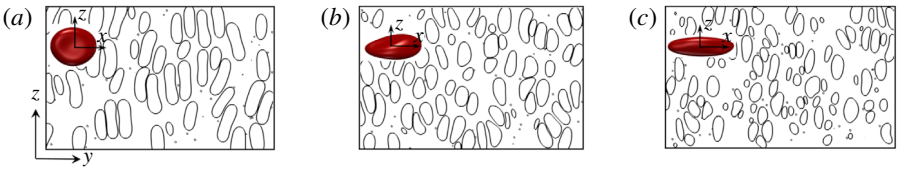


FIGURE 10. (Colour online) RBC and NP distributions and morphology in the cross-stream plane (y–z) with (*a*) $Ca_G = 0.055$, (*b*) $Ca_G = 0.55$ and (*c*) $Ca_G = 1.1$ at $Pe = 0.066$ and $\phi = 0.4$. Large non-circular disks are RBC cross-sectional contours. Small circles are NP cross-sectional contours. The $\bar{a}_{2,yz}$ value can be estimated from the PPDF analysis.

effective RBC size (i.e. the length scale $\bar{a}_{2,yz}$) and hence a decrease of the effective $\widetilde{Pe}$ in cross-stream directions. This explains the sublinear shear-rate scaling of the cross-stream RESID when increasing Ca_G. Likewise, the superlinear shear-rate scaling of the longitudinal RESID can be attributed to the elongation of RBC in the streamwise direction, i.e. the increase of the RESID length scale in the longitudinal direction. The change of the RESID length scales in different principal directions due to shear is the root cause of the nonlinear shear-rate dependence of the NP diffusion tensor.

3.7. *Empirical correlations*

In this section, we construct empirical correlations for the long-time NP diffusion tensor in sheared blood based on the scaling observations in the previous sections. Since all RESID coefficients scale linearly with $\widetilde{Pe}$ at fixed Ca_G, and the nonlinear shear-rate dependence of RESID is primarily due to the variation of Ca_G, as demonstrated in §§ 3.5 and 3.6, there hence exists a scaling relation, $\hat{D}^R_{ij} \sim O(\phi^{p_1}\widetilde{Pe}Ca_G^{p_2})$, such that the exponents p_1 and p_2 can be estimated through matching the nonlinear ϕ and $\dot{\gamma}$ scalings, respectively, as observed in § 3.3. Therefore, empirical correlations of NP long-time diffusivities can be constructed as functions of ϕ, $\widetilde{Pe}$ and Ca_G in the haemorheological range of $10 \leqslant \dot{\gamma} \leqslant 2000$ s^{-1} and $0.1 \leqslant \phi \leqslant 0.4$ as follows:

$$\frac{D^\infty_{xx}}{D^B} = \begin{cases} 1 + \mathcal{C}^l_{xx}\phi\widetilde{Pe}, & 0.0055 \leqslant Ca_G \leqslant 0.055, \\ 1 + \mathcal{C}^h_{xx}\phi^{Ca_G+0.945}\widetilde{Pe}Ca_G^{0.8}, & 0.055 < Ca_G \leqslant 1.10, \end{cases} \tag{3.4a}$$

$$\frac{D^\infty_{yy}}{D^B} = \begin{cases} 1 + \mathcal{C}^l_{yy}\phi\widetilde{Pe}, & 0.0055 \leqslant Ca_G \leqslant 0.055, \\ 1 + \mathcal{C}^h_{yy}\phi\widetilde{Pe}Ca_G^{-0.3}, & 0.055 < Ca_G \leqslant 1.10, \end{cases} \tag{3.4b}$$

$$\frac{D^\infty_{zz}}{D^B} = \begin{cases} 1 + \mathcal{C}^l_{zz}\phi\widetilde{Pe}, & 0.0055 \leqslant Ca_G \leqslant 0.055, \\ 1 + \mathcal{C}^h_{zz}\phi^{1.022-0.4Ca_G}\widetilde{Pe}Ca_G^{-0.2}, & 0.055 < Ca_G \leqslant 1.10, \end{cases} \tag{3.4c}$$

$$\frac{D^\infty_{xy}}{D^B} = \frac{D^\infty_{yx}}{D^B} = \begin{cases} \mathcal{C}^l_{xy}, & 0.0055 \leqslant Ca_G \leqslant 0.055, \\ \mathcal{C}^h_{xy}\phi\widetilde{Pe}, & 0.055 < Ca_G \leqslant 1.10, \end{cases} \tag{3.4d}$$

where $\mathcal{C}^q_{ij}$ with $q \in \{l, h\}$ are constants fitting the correlation values with the simulation measurements at low or high shear rates. The dimensional NP diffusion tensor can then be written in terms of the conventional shear-induced diffusion scaling, $O(\dot{\gamma}a_2^2)$, as

$$\boldsymbol{D}^\infty = D^B\boldsymbol{I} + \phi\dot{\gamma}a_2^2\boldsymbol{M}^q, \tag{3.5}$$

https://doi.org/10.1017/jfm.2019.320 Published online by Cambridge University Press

$\mathcal{C}^l_{xx}$	$\mathcal{C}^h_{xx}$	$\mathcal{C}^l_{yy}$	$\mathcal{C}^h_{yy}$	$\mathcal{C}^l_{zz}$	$\mathcal{C}^h_{zz}$	$\mathcal{C}^l_{xy}$	$\mathcal{C}^h_{xy}$
0.281	2.86	0.0432	0.0181	0.0241	0.0135	0	−0.0332

TABLE 4. Correlation constants for the empirical correlations of NP diffusion tensor in sheared cellular blood flow.

where the anisotropic tensor, $\boldsymbol{M}^q$, according to the severity of the RBC deformability ($Ca_G = \mu\dot{\gamma}a_2/G$) at different level of shear rates, yields piecewise expressions:

$$\boldsymbol{M}^l = \begin{pmatrix} \mathcal{C}^l_{xx} & \mathcal{C}^l_{xy} & 0 \\ \mathcal{C}^l_{yx} & \mathcal{C}^l_{yy} & 0 \\ 0 & 0 & \mathcal{C}^l_{zz} \end{pmatrix}, \quad 10 \leqslant \dot{\gamma} \leqslant 100\ \mathrm{s}^{-1}, \tag{3.6a}$$

$$\boldsymbol{M}^h = \begin{pmatrix} \mathcal{C}^h_{xx}\phi^{Ca_G-0.055}Ca_G^{0.8} & \mathcal{C}^h_{xy} & 0 \\ \mathcal{C}^h_{yx} & \mathcal{C}^h_{yy}/Ca_G^{0.3} & 0 \\ 0 & 0 & \mathcal{C}^h_{zz}/(\phi^{2Ca_G+0.11}Ca_G)^{0.2} \end{pmatrix}, \quad 100 < \dot{\gamma} \leqslant 2000\ \mathrm{s}^{-1}, \tag{3.6b}$$

where $\boldsymbol{M}^q$ quantifies the anisotropic behaviour of the NP diffusion tensor and characterizes its departure from the conventional shear-induced diffusion scaling, $O(\dot{\gamma}a_2^2)$, due to the presence of the deformable RBC phase. Table 4 lists all the constants, $\mathcal{C}^q_{ij}$. Each constant is obtained by calculating the slope of the best linear fit to the dataset, $(D^{(R,m)}_{ij}, D^{(R,th)}_{ij}/\mathcal{C}^q_{ij})$, for specific i, j and q at various $\dot{\gamma}$ and ϕ. Here, $D^{(R,m)}_{ij} = D^{\infty}_{ij} - D^B\delta_{ij}$ denotes the measured RESID evaluated by the calculated D^{∞}_{ij} subtracted by the theoretical BD; $D^{(R,th)}_{ij} = \phi\dot{\gamma}a_2^2M^q_{ij}$ denotes the theoretical diffusivity based on the proposed empirical correlations. The $\mathcal{C}^l_{xy}$ value is set to zero given its small magnitude; and $\mathcal{C}^h_{xy}$ is negative, suggesting that the predominant direction of NP migration in the long-time regime is along the contractile flow direction under high shear flow (Foss & Brady 1999). For cases at $\dot{\gamma} < 10\ \mathrm{s}^{-1}$ and $\phi < 0.1$, $\boldsymbol{D}^{\infty}$ can be approximated by the isotropic Brownian diffusivity provided the small magnitude of the RESID.

Figure 11 plots the measured NP diffusivities (subtracted by BD) versus the theoretical estimation based on the empirical correlations. The good collapse of the diffusivity measurements on the $D^{(R,m)}_{ij} = D^{(R,th)}_{ij}$ line demonstrates the empirical correlations can well reproduce the numerically measured diffusivity tensor of NP in sheared blood.

4. Conclusions

The dispersion of NP in cellular blood flow under unbounded, homogeneous shear has been investigated over a wide range of shear rate and haematocrit using an LB–LD–SL multiscale complex blood flow solver. In the short-time regimes, NP dispersive anomalies are observed and attributed to the transient morphology and orientation change of RBCs under high shear and high haematocrit. In the long-time regimes, results for the long-time diffusivity in the velocity-gradient direction agree well with existing experimental data. The long-time NP diffusion tensor has been described as a function of shear rate and haematocrit with various power-law scalings.

https://doi.org/10.1017/jfm.2019.320 Published online by Cambridge University Press

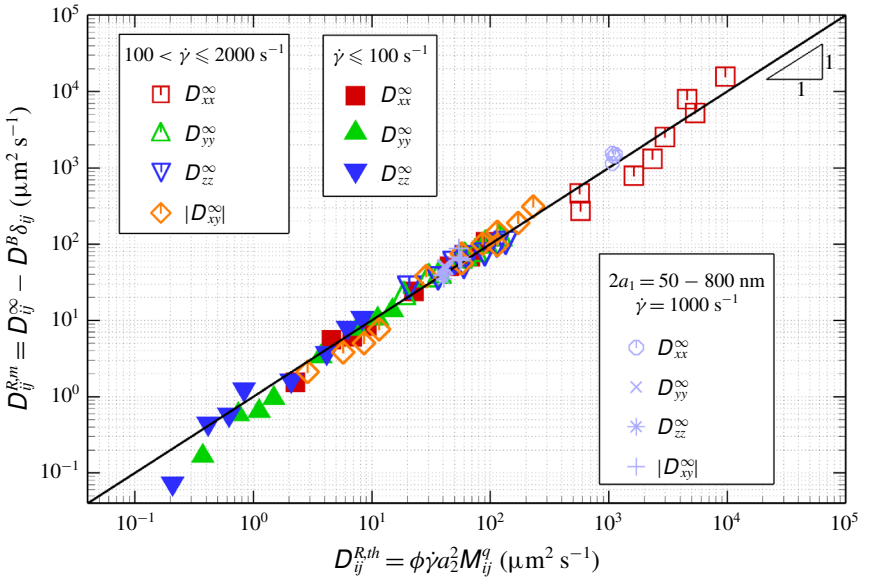


FIGURE 11. (Colour online) Measured NP RESID, $D^{(R,m)}_{ij} = D^{\infty}_{ij} - D^{B}\delta_{ij}$, as a function of the theoretical RESID, $D^{(R,th)}_{ij} = \phi\dot{\gamma}a_2^2 M^{q}_{ij}$, based on the empirical correlations presented in equations (3.6*a*) and (3.6*b*). For cases with $\dot{\gamma} \leqslant 100\ \mathrm{s}^{-1}$ (filled symbols), M^{l}_{ij} is applied to calculate $D^{(R,th)}_{ij}$. For cases with $\dot{\gamma} > 100\ \mathrm{s}^{-1}$ (open symbols), M^{h}_{ij} is applied to calculate $D^{(R,th)}_{ij}$.

By plotting the RBC–NP PPDF, the NP microstructure in sheared blood has been visualized for the first time, and features a rhombus configuration with a detailed inner structure that changes according to specific haemorheological conditions. The RBC–NP PPDF analysis also suggests a novel approach to visualizing the average RBC morphology in concentrated RBC suspensions subject to different haemorheological conditions. Under high shear rate, the ϕ^2 dependence in $\hat{D}^{R}_{xx}$ is proposed to be related to the x elongation of RBC and elevated RBC–NP PPDF near the fore–aft region, which together suggests possible more-than-two-body interaction occurring particularly in the streamwise direction. The sublinear ϕ dependence is suggested to be related to the reduced effective ϕ due to the substantial contraction of RBC in the vorticity direction subject to high shear. The RBC–NP bidisperse suspension presents an example of a highly anisotropic microstructure of particle suspensions caused by the compound effect of particle shape/orientation anisotropy and shear-flow anisotropy.

It is also found that there exists a critical shear rate ($\sim$100 s^{-1}) around which the RESID shear-rate dependence changes from linear to nonlinear scale. Through numerical experiments, the transition to nonlinear shear-rate scaling of RESID has been related to the prominent change of average RBC morphological state between different shear rates. Specifically, the superlinear scalings ($\dot{\gamma}^{1-1.8}$) of $\hat{D}^{R}_{xx}$ are due to the streamwise elongation of RBCs, while the sublinear scalings ($\dot{\gamma}^{0.7-0.8}$) of $\hat{D}^{R}_{yy}$ and $\hat{D}^{R}_{zz}$ are associated with the cross-stream contraction of RBCs (in response to the streamwise elongation). The morphological changes under shear alter the RESID

https://doi.org/10.1017/jfm.2019.320 Published online by Cambridge University Press

length scale in different principal directions, which has been demonstrated to be the fundamental cause of the nonlinear shear-rate dependence of the RESID. This mechanism is also worth distinguishing from the causes of the nonlinear shear-rate scaling of the self-diffusivity of RBCs (Gross *et al.* 2014; Mountrakis *et al.* 2016) or deformable capsules (Clausen *et al.* 2011), where the latter has been attributed to the heterogeneous interparticle 'collision' due to the cell deformability (Kumar & Graham 2012). However, the nonlinear shear-rate dependence of NP diffusion in sheared blood, based on our interrogation, is more associated with a 'one-way' mechanism, i.e. the RBC morphological adaptation to shear flow changes the RESID length scale, which further alters the NP diffusion rate.

The determination of the rescaled Péclet number being a more general non-dimensional term to describe the severity of RESID enables the comparison between the bidisperse NP–RBC suspension and the monodisperse colloidal suspensions. In the latter scenario where the particle size ratio is one, $\widetilde{Pe}$ drops to Pe and 'RESID' drops to the particle self-diffusivity. The self-diffusion tensor reported by Foss & Brady (1999) in a sheared monodisperse colloidal suspension is plotted in figure 9(*c*) for comparison. In both monodisperse and bidisperse scenarios, $\hat{D}^R_{xx}$ shows the greatest magnitude among all diffusivity terms; and $\hat{D}^R_{yy}$ is slightly greater than $\hat{D}^R_{zz}$. In general, $\hat{D}^R_{ij}$ in RBC–NP suspension shows higher anisotropy than the monodisperse case owing to the geometric asymmetry of RBCs (x being greater than y and z dimensions). Such a geometric asymmetry effect can be further increased with Ca_G, leading to higher anisotropy of the diffusivity tensor. In the monodisperse scenario, $\hat{D}^R_{xy}$ is the smallest; while in the NP–RBC bidisperse scenario, $\hat{D}^R_{xy}$ is greater than $\hat{D}^R_{yy}$ and $\hat{D}^R_{zz}$ due to the severe diffusive effect in the x direction.

This work, to the authors' knowledge, offers the first detailed study of the complete 3D NP diffusion tensor in cellular blood flow over a wide range of shear rates and haematocrits. The proposed empirical correlations for the NP diffusion tensor offers a constitutive relation that can be adopted by effective continuum models to pursue large-scale NP biotransport applications (e.g. *in vivo* NP drug delivery) with better accuracy.

Acknowledgements

The authors acknowledge the support from Sandia National Laboratories under grant 2506X36 and the computational resource provided by National Science Foundation under grant TG-CT100012. The authors appreciate the suggestion by one of the reviewers to consider the pair distribution function of NPs around RBCs in all three planes. Z.L. acknowledges the constructive discussions with Dr J. B. Lechman, Professor E. C. Eckstein and Professor K. B. Wiesenfeld. Sandia National Laboratories is a multimission laboratory managed and operated by National Technology and Engineering Solutions of Sandia LLC, a wholly owned subsidiary of Honeywell International Inc. for the US Department of Energy's National Nuclear Security Administration under contract DE-NA0003525. This paper describes objective technical results and analysis. Any subjective views or opinions that might be expressed in the paper do not necessarily represent the views of the US Department of Energy or the United States Government.

Supplementary movies

Supplementary movies are available at https://doi.org/10.1017/jfm.2019.320.

https://doi.org/10.1017/jfm.2019.320 Published online by Cambridge University Press

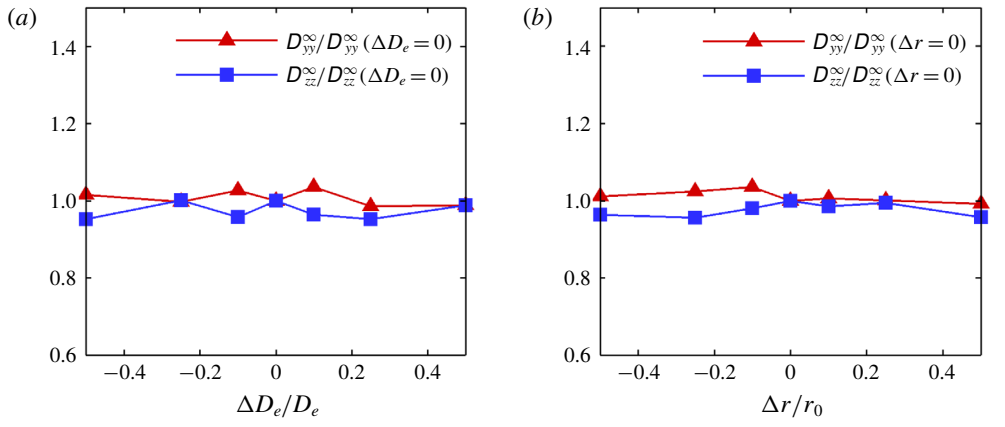


FIGURE 12. (Colour online) (*a*) NP long-time diffusivities in the cross-stream directions plotted against the relative variation of the Morse potential well depth (*a*) and equilibrium distance (*b*).

Appendix A. Sensitivity to NP–RBC contact model

The NP–RBC short-distance interaction is through a Morse potential that forbids NP from penetrating the RBC membrane. The potential parameters are adjusted to match the measured inter-cell potential energy, as discussed in Liu *et al.* (2004). The Morse potential function is given as

$$U_M(r) = D_e[\mathrm{e}^{-2\beta(r-r_0)} - 2\mathrm{e}^{-\beta(r-r_0)}] \quad (r \leqslant r_0), \tag{A 1}$$

where r is the normal distance between the particle centre to the RBC surface, r_0 is a cutoff distance in which no interaction forces are present, D_e is the potential well depth and β is a scaling factor. The surface energy is set to $D_e = 1 \times 10^7 k_B T$ and the equilibrium distance is set to $r_0 = a_1 + 10$ nm. In figure 12, we explore the sensitivity of the NP diffusivity calculation to the adjustment of the Morse model parameters. Figures 12(*a*) and 12(*b*) show that the D^{∞}_{yy} and D^{∞}_{zz} calculation exhibits less than 5 % variation when changing the magnitude of the energy and equilibrium distance, respectively, by up to ±60 %. This indicates that the NP diffusion is largely driven by the hydrodynamic interaction rather than by the direct contact between NP and RBC membrane.

Appendix B. Calculation of the partial pair distribution function

In the bidisperse RBC–NP suspension system, the NP–RBC partial pair distribution function (PPDF), $g_{21}(\boldsymbol{r})$, quantifies the conditional probability of finding an NP (species 1) at a position of $\boldsymbol{r}$ with respect to the geometric centre of a single RBC (species 2). This quantity can be calculated as

$$g_{21}(\boldsymbol{r}) = \frac{1}{n_2}\left\langle \sum_{i\in LB}\sum_{j\in b} \frac{\delta(\boldsymbol{r} - \boldsymbol{r}_2^i + \boldsymbol{r}_1^j)}{n_1^i L_b^3} \right\rangle, \tag{B 1}$$

where L_b defines the cubic box size for PPDF sampling around one RBC, index j goes through all NPs within the local sampling box, and i goes through all RBCs in

https://doi.org/10.1017/jfm.2019.320 Published online by Cambridge University Press

the computational LB domain. Notation r_2^i and r_1^j denotes the positions of RBC and NP, respectively; n_1^i shows the number concentration of NP within the sampling box; while n_2 denotes the number concentration of RBC in the entire domain. The angle brackets represent the ensemble average among independent realizations, which in the current case is through time averaging given the ergodic hypothesis. Similar techniques have recently been used in calculating PPDFs in bidisperse and polydisperse rigid-particle suspensions (Wang & Brady 2016; Pednekar *et al.* 2018). Projection of $g_{21}(\boldsymbol{r})$ to principal planes follows the integration procedure discussed in Kumar & Higdon (2011) but with a smaller integration interval, $(-a_2/4, a_2/4)$, to better capture the RBC morphological change.

The PPDF sampling box size for all cases is selected to be three times the RBC maximum diameter at equilibrium in biconcave shape, i.e. $L_b = 24$ μm. To capture the PPDF in the long-time regime ($t\dot{\gamma} > 100$) with detailed suspension microstructure, a total number of 300 strain units are employed for time averaging. In the short-time regime ($t\dot{\gamma} \sim 1$), owing to limited time steps associated with specific suspension configuration (e.g. the string ordered configuration), approximately three strain units are adopted for averaging.

REFERENCES

AHLRICHS, P. & DÜNWEG, B. 1998 Lattice-Boltzmann simulation of polymer–solvent systems. *Intl J. Mod. Phys.* C **09** (08), 1429–1438.

AHLRICHS, P. & DÜNWEG, B. 1999 Simulation of a single polymer chain in solution by combining lattice Boltzmann and molecular dynamics. *J. Chem. Phys.* **111** (17), 8225–8239.

AHMED, F., MEHRABADI, M., LIU, Z., BARABINO, G. A. & AIDUN, C. K. 2018 Internal viscosity-dependent margination of red blood cells in microfluidic channels. *J. Biomech. Engng* **140** (6), 061013.

AIDUN, C. K. & CLAUSEN, J. R. 2010 Lattice-Boltzmann method for complex flows. *Annu. Rev. Fluid Mech.* **42** (1), 439–472.

AIDUN, C. K. & LU, Y. 1995 Lattice Boltzmann simulation of solid particles suspended in fluid. *J. Stat. Phys.* **81** (1-2), 49–61.

AIDUN, C. K., LU, Y. N. & DING, E. J. 1998 Direct analysis of particulate suspensions with inertia using the discrete Boltzmann equation. *J. Fluid Mech.* **373**, 287–311.

AIDUN, C. K. & QI, D. W. 1998 A new method for analysis of the fluid interaction with a deformable membrane. *J. Stat. Phys.* **90** (1), 145–158.

ALBANESE, A., TANG, P. S. & CHAN, W. C. 2012 The effect of nanoparticle size, shape, and surface chemistry on biological systems. *Annu. Rev. Biomed. Engng* **14**, 1–16.

ANTONINI, G., GUIFFANT, G., QUEMADA, D. & DOSNE, A. M. 1978 Estimation of platelet diffusivity in flowing blood. *Biorheology* **15** (2), 111–117.

BHATNAGAR, P. L., GROSS, E. P. & KROOK, M. 1954 A model for collision processes in gases. I. Small amplitude processes in charged and neutral one-component systems. *Phys. Rev.* **94** (3), 511–525.

BLANCO, E., SHEN, H. & FERRARI, M. 2015 Principles of nanoparticle design for overcoming biological barriers to drug delivery. *Nat. Biotechnol.* **33** (9), 941–951.

BRADY, J. F. & MORRIS, J. F. 1997 Microstructure of strongly sheared suspensions and its impact on rheology and diffusion. *J. Fluid Mech.* **348**, 103–139.

BREEDVELD, V., VAN DEN ENDE, D., TRIPATHI, A. & ACRIVOS, A. 1998 The measurement of the shear-induced particle and fluid tracer diffusivities in concentrated suspensions by a novel method. *J. Fluid Mech.* **375**, 297–318.

BROOK, R. D., RAJAGOPALAN, S., POPE, C. A. 3RD, BROOK, J. R., BHATNAGAR, A., DIEZ-ROUX, A. V., HOLGUIN, F., HONG, Y., LUEPKER, R. V., MITTLEMAN, M. A. *et al.* 2010 Particulate matter air pollution and cardiovascular disease: An update to the scientific statement from the american heart association. *Circulation* **121** (21), 2331–2378.

https://doi.org/10.1017/jfm.2019.320 Published online by Cambridge University Press

BUSTAMANTE, C., BRYANT, Z. & SMITH, S. B. 2003 Ten years of tension: single-molecule DNA mechanics. *Nature* **421** (6921), 423–427.

CASA, L. D. C. & KU, D. N. 2017 Thrombus formation at high shear rates. *Annu. Rev. Biomed. Engng* **19** (1), 415–433.

CLAUSEN, J. R. & AIDUN, C. K. 2010 Capsule dynamics and rheology in shear flow: particle pressure and normal stress. *Phys. Fluids* **22** (12), 123302.

CLAUSEN, J. R., REASOR, D. A. & AIDUN, C. K. 2010 Parallel performance of a lattice-Boltzmann/finite element cellular blood flow solver on the IBM Blue Gene/p architecture. *Comput. Phys. Commun.* **181** (6), 1013–1020.

CLAUSEN, J. R., REASOR, D. A. & AIDUN, C. K. 2011 The rheology and microstructure of concentrated non-colloidal suspensions of deformable capsules. *J. Fluid Mech.* **685** (2011), 202–234.

DA CUNHA, F. R. & HINCH, E. J. 1996 Shear-induced dispersion in a dilute suspension of rough spheres. *J. Fluid Mech.* **309**, 211–223.

DAO, M., LI, J. & SURESH, S. 2006 Molecularly based analysis of deformation of spectrin network and human erythrocyte. *Mater. Sci. Engng* C **26** (8), 1232–1244.

DECUZZI, P., GODIN, B., TANAKA, T., LEE, S. Y., CHIAPPINI, C., LIU, X. & FERRARI, M. 2010 Size and shape effects in the biodistribution of intravascularly injected particles. *J. Control. Release* **141** (3), 320–327.

DILLER, T. E., MIKIC, B. B. & DRINKER, P. A. 1980 Shear-induced augmentation of oxygen transfer in blood. *J. Biomech. Engng* **102** (1), 67–72.

DING, E. J. & AIDUN, C. K. 2003 Extension of the lattice-Boltzmann method for direct simulation of suspended particles near contact. *J. Stat. Phys.* **112** (3–4), 685–708.

ECKSTEIN, E. C. & BELGACEM, F. 1991 Model of platelet transport in flowing blood with drift and diffusion terms. *Biophys. J.* **60** (1), 53–69.

ECKSTEIN, E. C., BAILEY, D. G. & SHAPIRO, A. H. 1977 Self-diffusion of particles in shear flow of a suspension. *J. Fluid Mech.* **79** (01), 191–208.

FEDOSOV, D. A., CASWELL, B. & KARNIADAKIS, G. E. 2010 A multiscale red blood cell model with accurate mechanics, rheology, and dynamics. *Biophys. J.* **98** (10), 2215–2225.

FEDOSOV, D. A., PAN, W., CASWELL, B., GOMPPER, G. & KARNIADAKIS, G. E. 2011 Predicting human blood viscosity in silico. *Proc. Natl Acad. Sci. USA* **108** (29), 11772–11777.

FOSS, D. R. & BRADY, J. F. 1999 Self-diffusion in sheared suspensions by dynamic simulation. *J. Fluid Mech.* **401**, 243–274.

FOSS, D. R. & BRADY, J. F. 2000*a* Brownian dynamics simulation of hard-sphere colloidal dispersions. *J. Rheol.* **44** (3), 629–651.

FOSS, D. R. & BRADY, J. F. 2000*b* Structure, diffusion and rheology of Brownian suspensions by Stokesian dynamics simulation. *J. Fluid Mech.* **407**, 167–200.

GRABOWSKI, E. F., FRIEDMAN, L. I. & LEONARD, E. F. 1972 Effects of shear rate on the diffusion and adhesion of blood platelets to a foreign surface. *Ind. Engng Chem. Res.* **11** (2), 224–232.

GRIFFIN, M. T., ZHU, Y., LIU, Z., AIDUN, C. K. & KU, D. N. 2018 Inhibition of high shear arterial thrombosis by charged nanoparticles. *Biomicrofluidics* **12** (4), 042210.

GROSS, M., KRUGER, T. & VARNIK, F. 2014 Fluctuations and diffusion in sheared athermal suspensions of deformable particles. *Eur. Phys. Lett.* **108** (6), 68006.

GUO, Z., ZHENG, C. & SHI, B. 2002 Discrete lattice effects on the forcing term in the lattice Boltzmann method. *Phys. Rev.* E **65** (4), 046308.

HE, X., ZOU, Q., LUO, L. S. & DEMBO, M. 1997 Analytic solutions of simple flows and analysis of nonslip boundary conditions for the lattice Boltzmann BGK model. *J. Stat. Phys.* **87** (1–2), 115–136.

HOSSAIN, S. S., ZHANG, Y., LIANG, X., HUSSAIN, F., FERRARI, M., HUGHES, T. J. & DECUZZI, P. 2013 In silico vascular modeling for personalized nanoparticle delivery. *Nanomedicine* **8** (3), 343–357.

JUNK, M. & YONG, W.-A. 2003 Rigorous Navier–Stokes limit of the lattice Boltzmann equation. *Asymp. Anal.* **35**, 165–185.

https://doi.org/10.1017/jfm.2019.320 Published online by Cambridge University Press

KUBO, R. 1966 The fluctuation–dissipation theorem. *Rep. Prog. Phys.* **29** (1), 255.

KUMAR, A. & GRAHAM, M. D. 2012 Mechanism of margination in confined flows of blood and other multicomponent suspensions. *Phys. Rev. Lett.* **109** (10), 108102.

KUMAR, A. & HIGDON, J. J. L. 2010 Origins of the anomalous stress behavior in charged colloidal suspensions under shear. *Phys. Rev.* E **82**, 051401.

KUMAR, A. & HIGDON, J. J. L. 2011 Dynamics of the orientation behavior and its connection with rheology in sheared non-Brownian suspensions of anisotropic dicolloidal particles. *J. Rheol.* **55** (3), 581–626.

LEE, T. R., CHOI, M., KOPACZ, A. M., YUN, S. H., LIU, W. K. & DECUZZI, P. 2013 On the near-wall accumulation of injectable particles in the microcirculation: smaller is not better. *Sci. Rep.* **3**, 2079.

LEES, A. W. & EDWARDS, S. F. 1972 The computer study of transport processes under extreme conditions. *J. Phys.* C **5** (15), 1921–1928.

LIPOWSKY, H. H. 2005 Microvascular rheology and hemodynamics. *Microcirculation* **12** (1), 5–15.

LIU, Y., ZHANG, L., WANG, X. & LIU, W. K. 2004 Coupling of Navier–Stokes equations with protein molecular dynamics and its application to hemodynamics. *Intl J. Numer. Meth. Fluids* **46** (12), 1237–1252.

LIU, Z., ZHU, Y., RAO, R. R., CLAUSEN, J. R. & AIDUN, C. K. 2018 Nanoparticle transport in cellular blood flow. *Comput. Fluids* **172**, 609–620.

LIU, Z., ZHU, Y., LECHMAN, J. B., RAO, R. R., CLAUSEN, J. R. & AIDUN, C. K. 2019 Multiscale method based on coupled lattice-Boltzmann and Langevin-dynamics for direct simulation of nanoscale particle/polymer suspensions in complex flows. *Intl J. Numer. Meth. Fluids* (in press).

MACMECCAN, R. M., CLAUSEN, J. R., NEITZEL, G. P. & AIDUN, C. K. 2009 Simulating deformable particle suspensions using a coupled lattice-Boltzmann and finite-element method. *J. Fluid Mech.* **618**, 13–39.

MALYSHEVA, A., LOMBI, E. & VOELCKER, N. H. 2015 Bridging the divide between human and environmental nanotoxicology. *Nat. Nanotechnol.* **10** (10), 835–844.

MEHRABADI, M., KU, D. N. & AIDUN, C. K. 2015 A continuum model for platelet transport in flowing blood based on direct numerical simulations of cellular blood flow. *Ann. Biomed. Engng* **43** (6), 1410–1421.

MEHRABADI, M., KU, D. N. & AIDUN, C. K. 2016 Effects of shear rate, confinement, and particle parameters on margination in blood flow. *Phys. Rev.* E **93** (2), 023109.

MILLER, M. R., RAFTIS, J. B., LANGRISH, J. P., MCLEAN, S. G., SAMUTRTAI, P., CONNELL, S. P., WILSON, S., VESEY, A. T., FOKKENS, P. H. B., BOERE, A. J. F. *et al.* 2017 Inhaled nanoparticles accumulate at sites of vascular disease. *ACS Nano* **11** (5), 4542–4552.

MORRIS, J. F. & BRADY, J. F. 1996 Self-diffusion in sheared suspensions. *J. Fluid Mech.* **312**, 223–252.

MOUNTRAKIS, L., LORENZ, E. & HOEKSTRA, A. G. 2016 Scaling of shear-induced diffusion and clustering in a blood-like suspension. *Eur. Phys. Lett.* **114** (1), 14002.

MULLER, K., FEDOSOV, D. A. & GOMPPER, G. 2014 Margination of micro- and nano-particles in blood flow and its effect on drug delivery. *Sci. Rep.* **4**, 4871.

MYNAM, M., SUNTHAR, P. & ANSUMALI, S. 2011 Efficient lattice Boltzmann algorithm for Brownian suspensions. *Phil. Trans. R. Soc. Lond.* A **369** (1944), 2237–2245.

NEU, B. & MEISELMAN, H. J. 2002 Depletion-mediated red blood cell aggregation in polymer solutions. *Biophys. J.* **83** (5), 2482–2490.

NEWBY, D. E., MANNUCCI, P. M., TELL, G. S., BACCARELLI, A. A., BROOK, R. D., DONALDSON, K., FORASTIERE, F., FRANCHINI, M., FRANCO, O. H., GRAHAM, I. *et al.* 2015 Expert position paper on air pollution and cardiovascular disease. *Eur. Heart J.* **36** (2), 83–93b.

PEDNEKAR, S., CHUN, J. & MORRIS, J. F. 2018 Bidisperse and polydisperse suspension rheology at large solid fraction. *J. Rheol.* **62** (2), 513–526.

PESKIN, C. S. 2002 The immersed boundary method. *Acta Numerica* **11**, 479–517.

https://doi.org/10.1017/jfm.2019.320 Published online by Cambridge University Press

PIVKIN, I. V. & KARNIADAKIS, G. E. 2008 Accurate coarse-grained modeling of red blood cells. *Phys. Rev. Lett.* **101** (11), 118105.

POPEL, A. S. & JOHNSON, P. C. 2005 Microcirculation and hemorheology. *Annu. Rev. Fluid Mech.* **37**, 43–69.

REASOR, D. A., CLAUSEN, J. R. & AIDUN, C. K. 2012 Coupling the lattice-Boltzmann and spectrin-link methods for the direct numerical simulation of cellular blood flow. *Intl J. Numer. Meth. Fluids* **68** (6), 767–781.

REASOR, D. A., CLAUSEN, J. R. & AIDUN, C. K. 2013*a* Rheological characterization of cellular blood in shear. *J. Fluid Mech.* **726**, 497–516.

REASOR, D. A. JR, MEHRABADI, M., KU, D. N. & AIDUN, C. K. 2013*b* Determination of critical parameters in platelet margination. *Ann. Biomed. Engng* **41** (2), 238–249.

SHANG, L., NIENHAUS, K. & NIENHAUS, G. U. 2014 Engineered nanoparticles interacting with cells: size matters. *J. Nanobiotechnol.* **12** (1), 5.

SIEGLE, P., GOYCHUK, I. & HANGGI, P. 2010 Origin of hyperdiffusion in generalized Brownian motion. *Phys. Rev. Lett.* **105** (10), 100602.

SIEROU, A. & BRADY, J. F. 2004 Shear-induced self-diffusion in non-colloidal suspensions. *J. Fluid Mech.* **506** (506), 285–314.

WAGNER, A. J. & PAGONABARRAGA, I. 2002 Lees–Edwards boundary conditions for lattice Boltzmann. *J. Stat. Phys.* **107** (1/2), 521–537.

WANG, M. & BRADY, J. F. 2016 Spectral Ewald acceleration of Stokesian dynamics for polydisperse suspensions. *Comput. Phys.* **306**, 443–477.

WANG, N. H. L. & KELLER, K. H. 1985 Augmented transport of extracellular solutes in concentrated erythrocyte suspensions in Couette-flow. *J. Colloid Interf. Sci.* **103** (1), 210–225.

WU, J. & AIDUN, C. K. 2010 Simulating 3D deformable particle suspensions using lattice Boltzmann method with discrete external boundary force. *Intl J. Numer. Meth. Fluids* **62** (7), 765–783.

XUE, W. & GREST, G. S. 1990 Shear-induced alignment of colloidal particles in the presence of a shear flow. *Phys. Rev. Lett.* **64** (4), 419–422.

YEO, K. & MAXEY, M. R. 2010 Anomalous diffusion of wall-bounded non-colloidal suspensions in a steady shear flow. *Eur. Phys. Lett.* **92** (2), 24008.

YOO, J. W., IRVINE, D. J., DISCHER, D. E. & MITRAGOTRI, S. 2011 Bio-inspired, bioengineered and biomimetic drug delivery carriers. *Nat. Rev. Drug Discov.* **10** (7), 521–535.

ZHAO, H. & SHAQFEH, E. S. G. 2011 Shear-induced platelet margination in a microchannel. *Phys. Rev.* E **83**, 061924.

ZHAO, H., SHAQFEH, E. S. G. & NARSIMHAN, V. 2012 Shear-induced particle migration and margination in a cellular suspension. *Phys. Fluids* **24** (1), 011902.

ZIA, R. N. & BRADY, J. F. 2010 Single-particle motion in colloids: force-induced diffusion. *J. Fluid Mech.* **658**, 188–210.

ZYDNEY, A. L. & COLTON, C. K. 1988 Augmented solute transport in the shear flow of a concentrated suspension. *Hydrodynamics* **10** (1), 77–96.

https://doi.org/10.1017/jfm.2019.320 Published online by Cambridge University Press